PAPER

High-fidelity dynamics of piezoelectric covered metamaterial Timoshenko beams using the spectral element method

View the article online for updates and enhancements.

High-fidelity dynamics of piezoelectric covered metamaterial Timoshenko beams using the spectral element method

Guobiao Hu[1,2,3,*] , **Lihua Tang**[4] , **Yaowen Yang**[2,3,*] , **Dewen Yu**[2,5] and **Yunlong Zi**[6]

[1] Thrust of the Internet of Things, The Hong Kong University of Science and Technology (Guangzhou), Nansha, Guangzhou, Guangdong 511400, People's Republic of China
[2] School of Civil and Environmental Engineering, Nanyang Technological University, 50 Nanyang Avenue, Singapore 639798, Singapore
[3] State Key Laboratory of Structural Analysis for Industrial Equipment, Dalian University of Technology, Dalian 116081, People's Republic of China
[4] Department of Mechanical Engineering, University of Auckland, 20 Symonds Street, Auckland 1010, New Zealand
[5] Key Laboratory of Education Ministry for Modern Design and Rotor-Bearing System, School of Mechanical Engineering, Xi'an Jiaotong University, Xianning West Road, Xi'an 710049, People's Republic of China
[6] Thrust of Sustainable Energy and Environment, The Hong Kong University of Science and Technology (Guangzhou), Nansha, Guangzhou, Guangdong 511400, People's Republic of China

E-mail: guobiaohu@hkust-gz.edu.cn and cywyang@ntu.edu.sg

CrossMark

Abstract

Piezoelectric metamaterial beams have received enormous research interest for the applications of vibration attenuation and/or energy harvesting in recent years. This paper presents a generic modelling approach for predicting the high-frequency dynamics of piezoelectric metamaterial beams. The spectral element method (SEM) is used to derive the dynamic stiffness matrix of a composite piezoelectric beam segment. Boundary condition implementations are demonstrated. Both band structure and transmittance analyses are realized. Several case studies for piezoelectric metamaterial beams configured in different geometric/electrical forms are carried out. The corresponding finite element (FE) models are built for verification, and a comparison study with the transfer matrix method (TMM) is conducted. For the uniform configurations, an almost indistinguishable difference is noted between the theoretical and FE results. For the stepped configurations, only minor discrepancies are observed in the high-frequency responses. The improved robustness and stability of the SEM method compared to the TMM method are demonstrated. A further discussion has been provided to explain the cause of the high-frequency discrepancies: sudden changes in the cross-section of the beam result in the stress concentration effect and reduce the bending stiffness at the junction connection. Finally, the value of the high-fidelity modelling approach is reflected through a parametric-based optimization study towards merging the Bragg scattering and locally resonant band gaps in an example piezoelectric metamaterial beam to achieve a wide band gap.

---

* Authors to whom any correspondence should be addressed.

(Some figures may appear in colour only in the online journal)

1. Introduction

Metamaterials, as an emerging concept in the past two decades, have attracted lots of research attention [1–5]. Band gaps opened in metamaterials by the local resonance (LR) mechanism provide new ways for low-frequency vibration attenuation and noise reduction. In the most beginning, LRs in metamaterials were realized by mechanical oscillators designed in various forms [6–8]. Local resonant band gaps are usually very narrow [9–11]. Researchers have devoted enormous efforts to widening band gaps, such as designing innovative resonators to produce multiple band gaps [12–14] and introducing dynamic nonlinearities [15, 16]. For example, Tan *et al* [17] proposed a dual-resonator microstructure to achieve broadband effective mass negativity. The consequence is that the dual-resonator metamaterial produced two band gaps. Chen *et al* [18] used dual-resonators in suppressing the vibration of a sandwich beam. More importantly, they examined the dissipative effect on the vibration attenuation performance of the band gaps. Li *et al* [19] even extended dual-resonators to multi-resonators and considered the damping effect in their study. The results showed that carefully tuning the damping could improve the generated multiple band gaps. Lu *et al* [20] introduced novel two-degree-of-freedom (2DOF) resonators into a beam for flexural vibration suppression. The novel 2DOF resonator could conduct translational and rotational motions. The two rotational vibration modes of the 2DOF resonators induced two band gaps at low frequencies. Li *et al* [21] designed a two-dimensional metamaterial with local resonators having different types of resonances. Therefore, the metamaterial could unsurprisingly produce multiple band gaps. Khajehtourian and Hussein [22] investigated a metamaterial with nonlinearity arising from the large elastic deformation. They showed that the large deformation-induced nonlinearity might lead to the combination of Bragg scattering (BS) and LR band gaps. Fang *et al* [23] studied the wave propagation in a nonlinear metamaterial consisting of multi-atomic chains. In addition to linear band gaps, nonlinearity-induced chaotic bands were generated and could significantly widen the vibration suppression bandwidth. More research on the topic of designing broadband metamaterials can be found in [24–28].

Using the electromechanical coupling behaviour of smart materials, piezoelectric metamaterials with inductive or capacitive shunt circuits were proposed to generate electrically controllable band gaps [29–34]. By virtue of the high transformability of shunt circuits [35, 36], the band gaps of piezoelectric metamaterials are favourably tunable without the need to modify mechanical structures. Making band gaps tunable

and controllable also indicates the possibility of broadband vibration attenuation [37]. For the above reason, piezoelectric metamaterials have been widely studied. Chen *et al* [38] proposed to control the equivalent stiffness of a piezoelectric element that constitutes the spring of the local resonator by changing the shunted negative capacitance. The LR was still generated by the mechanical resonator but became controllable due to the introduction of the piezoelectric element. This idea was then experimentally validated by Zhu *et al* [39]. Rather than tuning the equivalent stiffness, the internal capacitance of a piezoelectric element together with a shunt inductor can generate *L-C* resonance. Due to the electromechanical coupling effect, the *L-C* resonance can also induce a band gap. Thorp *et al* [29] performed an early study using periodic piezoelectric patches to attenuate the longitudinal wave propagation in a rod. Starting from the constitutive equations of piezoelectric materials and using the transfer matrix method (TMM), they developed a theoretical model to predict the band gap behaviours. Chen *et al* [40] improved the theoretical model by discarding some inappropriate assumptions adopted in [29]. Their result matched better with the finite element (FE) simulation result.

In terms of transverse wave propagation prohibition, Chen *et al* [41] presented a study of attaching piezoelectric patches periodically on a beam for bending vibration control. By representing the equivalent Young's modulus of the piezoelectric material as a function of the shunted impedance and still based on the TMM, they derived a theoretical model of that piezoelectric metamaterial beam. However, there lacks a direct verification by comparing with the FE result as in [41]. Yi and Collet [42] investigated a similar piezoelectric metamaterial beam and attempted to enlarge the band gap by introducing negative capacitances. However, the transmissibility result comparison revealed a noticeable error in the theoretical model. They pointed out that it was because the analytical formula overestimated the internal capacitance of the piezoelectric patch. In recent, Wang *et al* [43] also modelled a similar piezoelectric metamaterial beam, but still obvious discrepancies were observed in their results compared to FE-simulated ones. For a similar piezoelectric metamaterial beam but using a different modelling strategy, Sugino *et al* [44] proposed an approach to fast estimate the band gap bounds. Bao *et al* [45] designed a piezoelectric metamaterial beam with nonlinear electrical shunt circuit. Their results showed that introducing the nonlinear shunt circuits could broaden the BS band gaps. Other relevant studies on similar piezoelectric metamaterial beams and using similar modelling techniques can be found in [46–49]. The commonalities shared by the above works in their theoretical modelling include: (1) the beam

is modelled using the Euler–Bernoulli theory; (2) equivalent Young's modulus of the piezoelectric material is represented; (3) the TMM is adopted.

Note that circuit resonances are usually at high frequencies compared to their mechanical counterparts, implying that the band gaps of piezoelectric metamaterial beams are often formed in high-frequency ranges [50, 51]. Therefore, it is obvious that Timoshenko's beam theory [52] is more suitable for dealing with piezoelectric metamaterial beams. In addition to metamaterials, extensive research has been conducted on piezoelectric composite beams for various applications, employing different modelling methods. One such method is the spectral element method (SEM). Lee and Kim [53] first applied the SEM in analysing the dynamics of piezoelectric material-covered beams. Park and Lee [54] developed an SEM for piezoelectric composite beams by considering axial-bending movement coupling. They verified their model by comparing it with a corresponding FE model. Lee *et al* [55] further improved the spectral element model by incorporating Timoshenko's beam theory to investigate bending waves in composite beams. Wang [56] employed the SEM to model a piezoelectric beam energy harvester and emphasized the necessity of using Timoshenko's beam theory for thick/short piezoelectric beams. Li and Liu [57] applied the SEM to model a frame structure composed of piezoelectric rods and successfully suppressed vibrations in the structure using active control techniques. Wu *et al* [58] applied the SEM to study a complex lattice structure with embedded piezoelectric materials without using active control techniques. Jang *et al* [59] employed the SEM to study guided waves in thick beams with bonded piezoelectric patches. Abad and Rouzegar [60] extended the SEM to analyse the dynamics of piezoelectric composite plates. Ren *et al* [61] used the SEM to model periodic composite phononic beams, enabling active tuning of BS band gaps. Other relevant works utilizing the SEM for modelling piezoelectric composites can be found in [62–65].

According to the literature review, we noticed that while the SEM is a well-established method, its applications in modelling and analysing LR piezoelectric metamaterials with shunted circuits remain rare. This highlights a research gap in the field, and our study aims to address this by applying the SEM to the modelling and analysis of such LR piezoelectric metamaterials with shunted circuits. In this paper, we present a high-accuracy modelling method for piezoelectric metamaterial beams. In section 2, the mathematical formulation of the proposed method will be introduced. Timoshenko's beam theory is adopted to improve prediction accuracy in the high-frequency range. An independent circuit governing equation is established to fully consider the electromechanical coupling effect rather than wrapping up the electrical impedance into the equivalent Young's modulus formula. In addition, instead of the TMM, the SEM is adopted. Section 3 presents several case studies. Rigorous comparisons with their corresponding FE models will be demonstrated to verify the proposed modelling method. Regarding the accuracy issue and the potential value of this high-accuracy method, section 4 provides some further discussions and a parametric case study. Finally, concluding remarks are summarized in section 5.

2. Mathematical formulation

This section presents an overview of the piezoelectric metamaterial system to be investigated and develops the mathematical formulation to pave the way for facilitating the relevant analyses.

2.1. Model description

Figure 1 shows the schematic of a piezoelectric beam model that many researchers have widely explored and investigated. The beam structure consists of three layers. The top and bottom layers are piezoelectric materials. The middle layer is the substrate material that does not have the piezoelectric effect. The surfaces of the piezoelectric layers are disposed with electrode pairs in a periodic manner. Hence, the electrode treatment divides the beam into segments, but which are not physically broken up from the mechanics point of view. Each electrode pair is shunted to an independent inductive circuit with identical parameters as the others. Though the inductive circuit may be a synthesis of multiple electrical components with a resistive characteristic [66], we temporarily assume it only contains an inductor for simplicity. Each electrode segment we defined, together with the shunt circuit, constitutes a unit cell of the metamaterial. This paper focuses on developing a general and versatile modelling approach with higher accuracy. We will start with the most typical model, as shown in figure 1. More complicated configurations and models will be demonstrated and discussed in later sections.

There exist several different ways to make the connection of the two piezoelectric layers in each unit cell with the external inductive circuit. As there are two piezoelectric layers, it is natural to come up with the idea of connecting them in series or parallel. It is also worth noting the piezoelectric polarization issue. Different piezoelectric polarization situations require distinct circuit implantations to realize either in-series or -parallel connections. Figure 2 shows the close-up view of a unit cell that is implemented with various shunt circuit configurations. Though circuit implantations are different for different piezoelectric polarization situations, as long as they belong to the same type of configuration, i.e. in-series or in-parallel configuration, they will exhibit exactly the same macroscopic behaviour in dynamics.

2.2. Governing equations based on Hamilton's principle

Accurately modelling the behaviour of the piezoelectric material is of the utmost importance in this problem. Therefore, we begin with the constitutive law of piezoelectric materials under the linear assumption. According to the prevailing standard on piezoelectricity [67], we can use the below equations to describe the coupling between the elastic and electrostatic properties of the piezoelectric material:

$$\begin{bmatrix} \varepsilon_p \\ \gamma_p \\ D_3 \end{bmatrix} = \begin{bmatrix} S_{11}^E & 0 & d_{31} \\ 0 & S_{55}^E & 0 \\ d_{31} & 0 & \varepsilon_{33}^T \end{bmatrix} \begin{bmatrix} \sigma_p \\ \tau_p \\ E_3 \end{bmatrix} \quad (1)$$
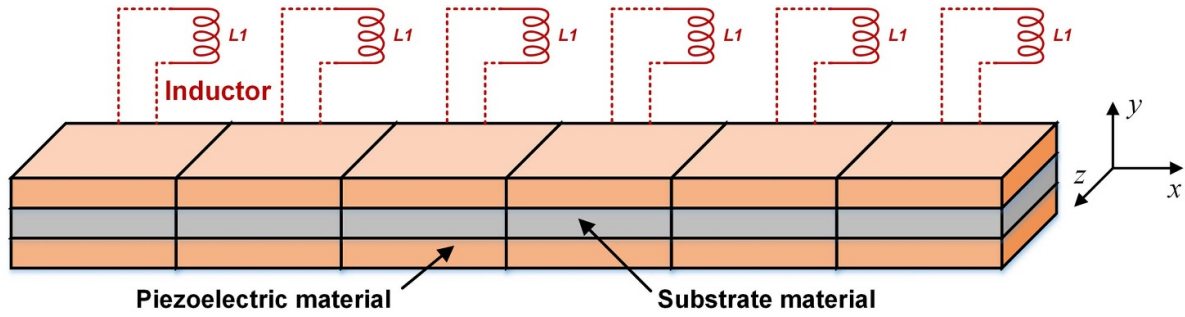
Figure 1. Schematic of a uniform piezoelectric metamaterial beam disposed with periodic electrode pairs and shunted to a series of identical inductive circuits. The orange and grey colours denote piezoelectric and substrate (brass in this paper) materials, respectively. Given a substrate segment, the piezoelectric segments on the top and bottom form a pair and connected in series/parallel, then shunted to an independent inductive circuit.
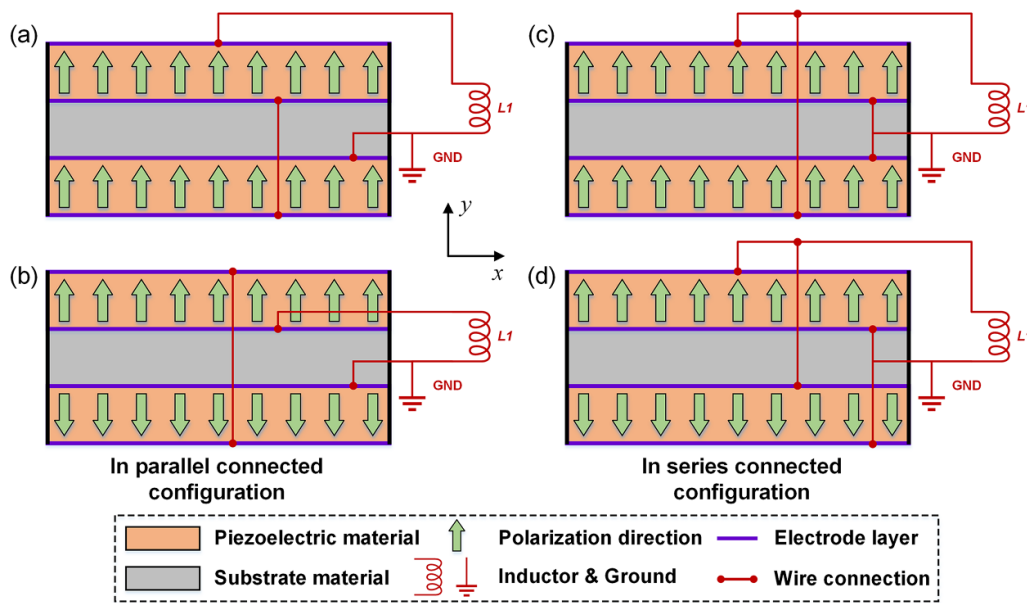

Figure 2. Close-up view of the shunt circuit connection. The top and bottom piezoelectric layers are connected in series, then shunted to the inductive circuit: (a) the top and bottom piezoelectric layers have the same polarization direction; and (b) the top and bottom piezoelectric layers have the opposite polarization directions. The top and bottom piezoelectric layers are connected in parallel, then shunted to the inductive circuit: (c) the top and bottom piezoelectric layers have the same polarization direction; and (d) the top and bottom piezoelectric layers have the opposite polarization directions.

where ε_p is the longitudinal strain in the beam length direction; γ_p is the shear strain in the beam thickness direction; σ_p and τ_p are the corresponding longitudinal and shear stresses, respectively; S_{11}^E and S_{55}^E are the elastic compliance constants; d_{31} is the piezoelectric constant in the unit of meter per volt (m V^{-1}); ε_{33}^T is the dielectric permittivity at constant stress; D_3 is the electric displacement in the direction normal to the beam surface; E_3 is the dielectric field in the beam thickness direction. The above equations described the strains as the functions of the stresses. Alternatively, we can express the stresses in terms of the strain components:

$$
\begin{bmatrix} \sigma_p \\ \tau_p \\ E_3 \end{bmatrix} = \begin{bmatrix} C_{11}^D & 0 & -h_{31} \\ 0 & C_{55}^D & 0 \\ -h_{31} & 0 & \beta_{33}^S \end{bmatrix} \begin{bmatrix} \varepsilon_p \\ \gamma_p \\ D_3 \end{bmatrix} \quad (2)
$$

where C_{11}^D and C_{55}^D are the elastic stiffness constants; h_{31} is the piezoelectric constant in the unit of voltage per meter (V m^{-1}); β_{33}^S is the permittivity constant. Equations (1) and (2) are equivalent to each other. Comparing the two equations, we note that the properties of a piezoelectric material can be fully determined by precisely defining $\{S_{11}^E, S_{55}^E, d_{31}, \varepsilon_{33}^T\}$ or $\{C_{11}^D, C_{55}^D, h_{31}, \beta_{33}^S\}$. The relationships between the two sets of material parameters can be derived as:

$$
\begin{cases} \beta_{33}^S = \dfrac{1}{\left(\varepsilon_{33}^T - d_{31}^2 / S_{11}^E\right)} & h_{31} = \beta_{33}^T d_{31} C_{11}^D \\ C_{11}^D = \dfrac{\left(1 / S_{11}^E\right)}{1 - d_{31}^2 \beta_{33}^T \left(1 / S_{11}^E\right)} & C_{55}^D = \dfrac{1}{S_{55}^E} \end{cases} \quad (3)
$$

where C_{55}^D takes the concise form as $1 / S_{55}^E$, since the shear-related piezoelectric effect is ignored by considering that d_{51} is usually much smaller than d_{31} and the shear strain component is much smaller than the longitudinal one. A bit unlike

the above definitions, in commercial FE software, such as COMSOL, one is required to input $\{S_{11}^E, S_{55}^E, d_{31}, \varepsilon_{33}^T\}$ which is termed as the strain-charge form, or $\{C_{11}^E, C_{55}^E, e_{31}, \varepsilon_{33}^S\}$ which is termed as the stress-charge form, for fully specifying the properties of a piezoelectric material. Since COMSOL models will be built to verify our theoretical models, the detailed transformation relations between the two sets of parameters are also given out as below:

$$\begin{cases} C_{11}^E = \frac{1}{S_{11}^E} & C_{55}^E = \frac{1}{S_{55}^E} \\ e_{31} = d_{31}C_{11}^E & \varepsilon_{33}^S = \varepsilon_{33}^T - d_{31}^2 / S_{11}^E \end{cases}. \tag{4}$$

Based on the constitutive equations (equation (2)), we can write down the stresses in the piezoelectric material in terms of the stain components:

$$\begin{cases} \sigma_p = C_{11}^D \varepsilon_p - D_3 h_{31} \\ \tau_p = C_{55}^D \gamma_p \end{cases}. \tag{5}$$

Moreover, under the small deflection assumption, the strain components in the piezoelectric material can be expressed as the functions of the transverse and rotational displacements:

$$\begin{cases} \varepsilon_p = -\frac{\partial \phi(x,t)}{\partial x}y \\ \gamma_p = \phi(x,t) - \frac{\partial w(x,t)}{\partial x} \end{cases} \tag{6}$$

where $w(x,t)$ is the transverse displacement of the beam, $\phi(x,t)$ is the rotation angle of the beam cross-section due to the shear deformation. The stress and strain components in the substrate material without piezoelectric effect take simpler forms as below:

$$\text{stress:} \begin{cases} \sigma_s = E_s \varepsilon_s \\ \tau_s = G_s \gamma_s \end{cases} \qquad \text{strain:} \begin{cases} \varepsilon_s = -\frac{\partial \phi(x,t)}{\partial x}y \\ \gamma_s = \phi(x,t) - \frac{\partial w(x,t)}{\partial x} \end{cases}. \tag{7}$$

The total potential energy of the piezoelectric composite beam can be obtained [55]:

$$V_{\text{potential}} = \frac{1}{2}\int_{V_s} (\sigma_s \varepsilon_s + \tau_s \gamma_s)\,\mathrm{d}V_s + \frac{1}{2}\int_{V_p} (\sigma_p \varepsilon_p + \tau_p \gamma_p + E_3 D_3)\,\mathrm{d}V_p \tag{8}$$

where the last term in the second integral of equation (8) represents the electric potential energy stored in the piezoelectric material. Substituting equations (5)–(7) into equation (8) yields:

$$V_{\text{potential}} = \frac{1}{2}\int_{x=0}^{L} \left\{ \begin{array}{l} \left[E_s I_s + 2C_{11}^D (I_p + A_p h_{pc})\right] \left[\frac{\partial \phi(x,t)}{\partial x}\right]^2 + \left(A_s G_s + 2A_p C_{55}^D\right) \left[-\frac{\partial w(x,t)}{\partial x} + \phi(x,t)\right]^2 \\ +2\left(A_p D_3^{\text{top}} h_{31}^{\text{top}} h_{pc} - A_p D_3^{\text{bot}} h_{31}^{\text{bot}} h_{pc}\right)\frac{\partial \phi(x,t)}{\partial x} + A_p \beta_{33}^S \left[\left(D_3^{\text{top}}\right)^2 + \left(D_3^{\text{bot}}\right)^2\right] \end{array} \right\} \mathrm{d}x \tag{9}$$

where $I_s = bh_s^3/12$, $A_s = bh_s$, $I_p = bh_p^3/12$, $A_p = bh_p$. Taking the variation of the potential energy gives [68]:

$$\begin{aligned} \delta V_{\text{potential}} &= \widehat{EI}\frac{\partial \phi(x,t)}{\partial x}\delta \phi(x,t)\bigg|_{x=0}^{L} - \int_{x=0}^{L} \widehat{EI}\frac{\partial^2 \phi(x,t)}{\partial x^2}\delta \phi(x,t)\,\mathrm{d}x \\ &+ \widehat{GA}\left[\frac{\partial w(x,t)}{\partial x} - \phi(x,t)\right]\delta w(x,t)\bigg|_{x=0}^{L} - \int_{x=0}^{L} \widehat{GA}\left[\frac{\partial^2 w(x,t)}{\partial x^2} - \frac{\partial \phi(x,t)}{\partial x}\right]\delta w(x,t)\,\mathrm{d}x \\ &+ \int_{x=0}^{L} \widehat{GA}\left[-\frac{\partial w(x,t)}{\partial x} + \phi(x,t)\right]\delta \phi(x,t)\,\mathrm{d}x + \int_{x=0}^{L} A_p \beta_{33}^S \left(D_3^{\text{top}}\delta D_3^{\text{top}} + D_3^{\text{bot}}\delta D_3^{\text{bot}}\right)\mathrm{d}x \\ &+ \int_{x=0}^{L} A_p h_{pc}\left(h_{31}^{\text{top}}\delta D_3^{\text{top}} - h_{31}^{\text{bot}}\delta D_3^{\text{bot}}\right)\phi(x,t)\,\mathrm{d}x + \int_{x=0}^{L} A_p h_{pc}\left(D_3^{\text{top}} h_{31}^{\text{top}} - D_3^{\text{bot}} h_{31}^{\text{bot}}\right)\delta \phi(x,t)\,\mathrm{d}x \end{aligned} \tag{10}$$

where $\widehat{EI} = E_s I_s + 2C_{11}^D \left(I_p + A_p h_{pc}\right)$, $\widehat{GA} = \left(A_s G_s + 2A_p C_{55}^E\right)$. The total kinetic energy of the piezoelectric composite beam can be written as:

$$T_{\text{kinetic}} = \frac{1}{2} \int\limits_{x=0}^{L} \left\{ b\left(h_s\rho_s + 2h_p\rho_p\right) \left(\frac{\partial w(x,t)}{\partial t}\right)^2 \right.$$
$$\left. + \left[\rho_s I_s + 2\rho_p\left(I_p + A_p h_{pc}\right)\right]\left(\frac{\partial \phi(x,t)}{\partial t}\right)^2 \right\} \mathrm{d}x. \quad (11)$$

The variation in the kinetic energy is:

$$\delta T_{\text{kinetic}} = \widehat{\rho A}\, \frac{\partial w(x,t)}{\partial t}\delta w(x,t)\bigg|_{x=0}^{L}$$
$$- \int_{x=0}^{L} \widehat{\rho A}\, \frac{\partial^2 w(x,t)}{\partial t^2}\delta w(x,t)\,\mathrm{d}x$$
$$+ \widehat{\rho I}\, \frac{\partial \phi(x,t)}{\partial t}\delta \phi(x,t)\bigg|_{x=0}^{L}$$
$$- \int_{x=0}^{L} \widehat{\rho I}\, \frac{\partial^2 \phi(x,t)}{\partial t^2}\delta \phi(x,t)\,\mathrm{d}x \quad (12)$$

where $\widehat{\rho A} = b\left(\rho_s + 2\rho_p\right)$, $\widehat{\rho I} = \rho_s I_s + 2\rho_p\left(I_p + A_p h_{pc}\right)$. The virtual work done by the external force and the applied electric field is:

$$\delta W_{\text{virtual}} = \int_{x=0}^{L} f_{\text{ext}}\delta w(x,t)\,\mathrm{d}x + \int_{x=0}^{L} M_{\text{ext}}\delta \phi(x,t)\,\mathrm{d}x$$
$$+ \int_{x=0}^{L} bv_{\text{top}}\delta D_3^{\text{top}}\mathrm{d}x + \int_{x=0}^{L} bv_{\text{bot}}\delta D_3^{\text{bot}}\mathrm{d}x \quad (13)$$

where f_{ext} and M_{ext} are the external force and moment applied on the piezoelectric metamaterial beam, respectively. Applying the extended Hamilton's principle and temporarily ignoring the external loadings, one can obtain the governing equations of the piezoelectric metamaterial beam:

$$\widehat{\rho A}\, \frac{\partial^2 w(x,t)}{\partial t^2} + \widehat{GA}\left[\frac{\partial \phi(x,t)}{\partial x} - \frac{\partial^2 w(x,t)}{\partial x^2}\right] = 0 \quad (14)$$

$$\widehat{\rho I}\, \frac{\partial^2 \phi(x,t)}{\partial t^2} + \widehat{GA}\left[\phi(x,t) - \frac{\partial w(x,t)}{\partial x}\right] - \widehat{EI}\, \frac{\partial^2 \phi(x,t)}{\partial x^2}$$
$$+ \left[\frac{A_p h_{pc}\left(h_{31}^{top}\right)^2}{\beta_{33}^S} + \frac{A_p h_{pc}\left(h_{31}^{bot}\right)^2}{\beta_{33}^S}\right]\frac{\partial^2 \phi(x,t)}{\partial x^2} = 0 \quad (15)$$

$$\begin{cases} D_3^{\text{top}} = -\left[\dfrac{h_{pc}h_{31}^{top}}{\beta_{33}^S}\dfrac{\partial \phi(x,t)}{\partial x} + \dfrac{v_{\text{top}}}{h_p\beta_{33}^S}\right] \\[3mm] D_3^{\text{bot}} = -\left[-\dfrac{h_{pc}h_{31}^{bot}}{\beta_{33}^S}\dfrac{\partial \phi(x,t)}{\partial x} + \dfrac{v_{\text{bot}}}{h_p\beta_{33}^S}\right] \end{cases}. \quad (16)$$

Equation (16) contains the general governing equations of the two piezoelectric layers operating independently. The electric charge collected by the electrodes can be obtained by integrating the electric displacement over the electrode area. If the top and bottom piezoelectric layers are connected in parallel (figures 2(a) and (b)), we have:

$$q(t) = b\int_0^L D_3^{\text{top}} + D_3^{\text{bot}}\mathrm{d}x$$
$$= -\left\{\frac{2bh_{pc}h_{31}}{\beta_{33}^S}\left[\phi(L,t) - \phi(0,t)\right] + \frac{2\varepsilon_{33}^S bL}{h_p}v(t)\right\}. \quad (17)$$

If the top and bottom piezoelectric layers are connected in series (figures 2(c) and (d)), we have:

$$q(t) = b\int_0^L D_3^{\text{top}}\mathrm{d}x$$
$$= -\left\{\frac{bh_{pc}h_{31}}{\beta_{33}^S}\left[\phi(L,t) - \phi(0,t)\right] + \frac{\varepsilon_{33}^S bL}{h_p}\frac{v(t)}{2}\right\}. \quad (18)$$

Assume the external shunt circuit is an inductive circuit, i.e. L_I, as shown in figure 3(a), the governing equation of the electrical domain for the in-parallel connection configuration can be written as:

$$\frac{\mathrm{d}i_p(t)}{\mathrm{d}t} = \frac{\mathrm{d}^2 q(t)}{\mathrm{d}t^2}$$
$$= -\left\{C_p\frac{\mathrm{d}^2 v(t)}{\mathrm{d}t^2} - \theta\left[\frac{\partial^2 \phi(L,t)}{\partial t^2} - \frac{\partial^2 \phi(0,t)}{\partial t^2}\right]\right\} = \frac{v(t)}{L_I} \quad (19)$$

where $C_p = 2\varepsilon_{33}^S bL/h_p$ is the equivalent capacitance of the in-parallel connected piezoelectric layers; $\theta = 2bh_{pc}d_{31}/S_{11}^E$. The governing equation of the electrical domain for the in-series connection configuration is in the exactly same form as equation (19), but $C_p = \varepsilon_{33}^S bL/2h_p$, which is the equivalent capacitance of the in-series connected piezoelectric layers and $\theta = bh_{pc}d_{31}/S_{11}^E$. However, a purely inductive circuit is difficult to obtain. Even an inductor component usually has a certain resistive feature. If the external shunt circuit has a parasitic resistor, as shown in figure 3(b), the governing equations of the circuit can be obtained as:

$$\begin{cases} i_p(t) = -\left\{C_p\dfrac{\mathrm{d}v(t)}{\mathrm{d}t} - \theta\left[\dfrac{\partial \phi(L,t)}{\partial t} - \dfrac{\partial \phi(0,t)}{\partial t}\right]\right\} \\[3mm] R_L i_p(t) + L_I\dfrac{\mathrm{d}i_p(t)}{\mathrm{d}t} = v(t) \end{cases}. \quad (20)$$
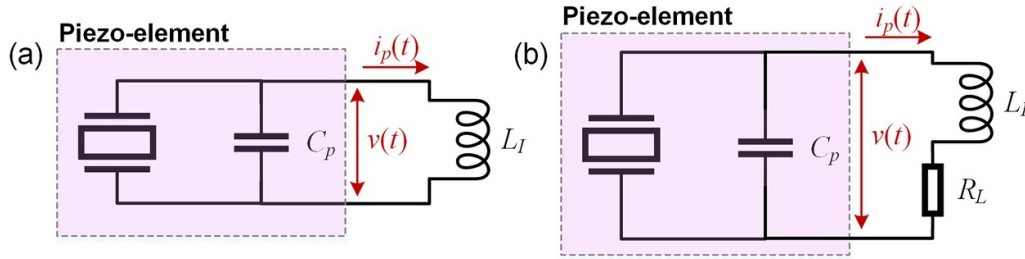
Figure 3. Schematic of the current flowing out of the piezoelectric element and the voltage difference across the piezoelectric element. The lumped piezoelectric element is a simplified representation of the two piezoelectric layers connected in series or parallel: (a) the external shunt circuit is only a single inductor; (b) the external shunt circuit consists of an inductor and a resistor in series.

2.3. Derivation of dynamic stiffness matrix

We consider the model is subjected to a harmonic excitation. Since only the steady-state harmonic responses are of interest, we can assume the solutions to equations (14)–(19) in the below form:

$$\begin{cases} w(x,t) = W(x) e^{i\omega t} \\ \phi(x,t) = \Phi(x) e^{i\omega t} \\ v(t) = V e^{i\omega t} \end{cases} \quad (21)$$

where $i = \sqrt{-1}$ is the imaginary number. By substituting the equation (21) into equations (14)–(19) and suppressing the time-harmonic dependence $e^{i\omega t}$, we can transform the governing equations into the frequency domain:

$$\widehat{GA}\left[\frac{\mathrm{d}\Phi(x)}{\mathrm{d}x} - \frac{\mathrm{d}^2 W(x)}{\mathrm{d}x^2}\right] - \omega^2 \widehat{\rho A} W(x) = 0 \quad (22)$$

$$-\omega^2 \widehat{\rho I}\,\Phi(x) + \widehat{GA}\left[\Phi(x) - \frac{\mathrm{d}W(x)}{\mathrm{d}x}\right] - EI\frac{\mathrm{d}^2\Phi(x)}{\mathrm{d}x^2} = 0 \quad (23)$$

$$-\omega^2 C_p V - \omega^2 \theta\left[\Phi(L) - \Phi(0)\right] = -\frac{V}{L_I} \quad (24)$$

where $EI = \widehat{EI}\frac{\partial^2\phi(x,t)}{\partial x^2} - \frac{2A_p h_{pc} h_{31}^2}{\beta_{33}^S}$. The general solutions to equations (22) and (23) are assumed to be:

$$\begin{cases} W(x) = B e^{ikx} \\ \Phi(x) = r B e^{ikx} \end{cases} . \quad (25)$$

It is noteworthy that the above general solutions apply to uniform beam segments covered by piezoelectric materials. In the subsequent case studies, we will examine models that involve plain beam segments without piezoelectric materials. The general solutions for plain beam segments without piezoelectric coverage can be assumed in the same forms, but the unknowns in the formulas are different. The beam needs to be divided into distinct segments at the locations where there are geometric or material discontinuities. Each

segment must be a uniform section to ensure the validity of the general solutions. Substituting the assumed solutions, i.e. equation (25), back into equations (22) and (23) yields an eigenvalue problem

$$\begin{bmatrix} k^2\widehat{GA} - \omega^2\widehat{\rho A} & ik\widehat{GA} \\ -ik\widehat{GA} & -\omega^2\widehat{\rho I} + k^2 EI + \widehat{GA} \end{bmatrix}\begin{bmatrix} 1 \\ r \end{bmatrix} = \begin{bmatrix} 0 \\ 0 \end{bmatrix}. \quad (26)$$

To ensure the existence of non-trivial solutions, the determinant of the coefficient matrix in equation (26) has to be zero. Thereby, we can determine the wavenumber k by solving the following polynomial function:

$$k^4 - \eta k_F^4 k^2 - k_F^4\left(1 - \eta_1 k_G^4\right) = 0 \quad (27)$$

where $k_F = \left(\frac{\omega^2\widehat{\rho A}}{EI}\right)^{\frac{1}{4}}$, $k_G = \left(\frac{\omega^2\widehat{\rho A}}{\widehat{GA}}\right)^{\frac{1}{4}}$, $\eta_1 = \widehat{\rho I}/\widehat{\rho A}$, $\eta_2 = EI/\widehat{GA}$, and $\eta = \eta_1 + \eta_2$. The four roots of equation (27) are:

$$\begin{cases} k_1 = \frac{1}{2}\sqrt{2\eta k_F^2 + 2\sqrt{\eta^2 k_F^4 - 4\eta_1 k_G^4 + 4}} \\ k_2 = \frac{1}{2}\sqrt{2\eta k_F^2 - 2\sqrt{\eta^2 k_F^4 - 4\eta_1 k_G^4 + 4}} \\ k_3 = -k_1 \\ k_4 = -k_2 \end{cases} . \quad (28)$$

Given the above four wavenumbers, we can rewrite the general solutions in equation (25) as below:

$$\begin{cases} W(x) = B_1 e^{ik_1 x} + B_2 e^{ik_2 x} + B_3 e^{-ik_1 x} + B_4 e^{-ik_2 x} \\ \Phi(x) = r_1 B_1 e^{ik_1 x} + r_2 B_2 e^{ik_2 x} - r_1 B_3 e^{-ik_1 x} - r_2 B_4 e^{-ik_2 x} \end{cases} \quad (29)$$

where $r_j = \frac{i\left(k_j^2 - k_G^4\right)}{k_j}$, $j = 1$ or 2. The nodal displacements of the piezoelectric metamaterial beam can be calculated by substituting the nodal coordinates into equation (29):

$$
\underbrace{\begin{bmatrix} W(0) \\ \Phi(0) \\ W(L) \\ \Phi(L) \end{bmatrix}}_{d} = \underbrace{\begin{bmatrix} 1 & 1 & 1 & 1 \\ r_1 & r_2 & -r_1 & -r_2 \\ e^{ik_1 L} & e^{ik_2 L} & e^{-ik_1 L} & e^{-ik_2 L} \\ r_1 e^{ik_1 L} & r_2 e^{ik_2 L} & -r_1 e^{-ik_1 L} & -r_2 e^{-ik_2 L} \end{bmatrix}}_{R} \underbrace{\begin{bmatrix} B_1 \\ B_2 \\ B_3 \\ B_4 \end{bmatrix}}_{B}.
\tag{30}
$$

The bending moment and transverse shear force distribution along a Timoshenko beam can be written as:

$$
\begin{cases} Q = \widehat{GA}\left[\dfrac{\partial W(x)}{\partial x} - \Phi(x)\right] \\ M = EI\dfrac{\partial \Phi(x)}{\partial x} \end{cases}.
\tag{31}
$$

The nodal forces and moments can also be related to the displacement fields by:

$$
\underbrace{\begin{bmatrix} -Q(0) \\ -M(0) \\ Q(L) \\ M(L) \end{bmatrix}}_{f} = \underbrace{\begin{bmatrix} -\widehat{GA}(-r_1+ik_1) & -\widehat{GA}(-r_2+ik_2) & -\widehat{GA}(r_1-ik_1) & -\widehat{GA}(r_2-ik_2) \\ -ir_1 k_1 EI & -ir_2 k_2 EI & -ir_1 k_1 EI & -ir_2 k_2 EI \\ \widehat{GA}(-r_1+ik_1)e^{ik_1 L} & \widehat{GA}(-r_2+ik_2)e^{ik_2 L} & \widehat{GA}(r_1-ik_1)e^{-ik_1 L} & \widehat{GA}(r_2-ik_2)e^{-ik_2 L} \\ ir_1 k_1 EI e^{ik_1 L} & ir_2 k_2 EI e^{ik_2 L} & ir_1 k_1 EI e^{-ik_1 L} & ir_2 k_2 EI e^{-ik_2 L} \end{bmatrix}}_{H} \underbrace{\begin{bmatrix} B_1 \\ B_2 \\ B_3 \\ B_4 \end{bmatrix}}_{B}.
\tag{32}
$$

Therefore, we can represent the nodal forces and moments by the nodal displacements:

$$
f = HR^{-1}d.
\tag{33}
$$

Noting that the piezoelectric materials will also generate bending moments due to the piezoelectric effect. The stress generated by the piezoelectric effect is:

$$
\sigma_p^E = -e_{31}E_3.
\tag{34}
$$

The superscript E denotes the electric field-induced stress component. The electric field can be further expressed as:

$$
E_3 = \begin{cases} \dfrac{v(t)}{h_p} & \text{in parallel connection} \\ \dfrac{v(t)}{2h_p} & \text{in series connection} \end{cases}.
\tag{35}
$$

The internal moment induced by the piezoelectric effect can be obtained by integrating the infinitesimal moment along the piezoelectric thickness:

$$
\begin{aligned}
M_p(x,t) &= -\left[\int_{h_s/2}^{h_s/2+h_p} b\sigma_p^E y\,\mathrm{d}y + \int_{-h_s/2-h_p}^{-h_s/2} b\sigma_p^E y\,\mathrm{d}y\right] \\
&= -2\left[\int_{h_s/2}^{h_s/2+h_p} -be_{31}\dfrac{v(t)}{h_p}y\,\mathrm{d}y\right] = \theta v(t).
\end{aligned}
\tag{36}
$$

Note that the expressions of θ varies for different connection configurations. By omitting the time-harmonic dependence, we can convert the above equation into the frequency domain:

$$
M_p = \theta V.
\tag{37}
$$

On the other hand, solving equation (24) gives:

$$
V = \Theta\left[\Phi(L) - \Phi(0)\right]
\tag{38}
$$

where $\Theta = \frac{\theta L_I \omega^2}{(C_p L_I \omega^2 - 1)}$ if the external shunt circuit contains only a single inductor (L_I); however, if the shunt circuit consists of an inductor (L_I) and a resistor (R_L) in series, as shown in figure 3(b), $\Theta = \frac{i\omega(R_L + i\omega L_I)}{i\omega C_p(R_L + i\omega L_I) + 1}$, which can be derived from equation (20). Subsequently, by substituting equation (38) into equation (37), we obtain:

$$
M_p = \Theta\theta\left[\Phi(L) - \Phi(0)\right].
\tag{39}
$$

Representing the piezoelectric effect induced bending moments by the nodal displacements yields:

$$
\underbrace{\begin{bmatrix} -Q_p(0) \\ -M_p(0) \\ Q_p(L) \\ M_p(L) \end{bmatrix}}_{f_p} = \underbrace{\begin{bmatrix} 0 & 0 & 0 & 0 \\ 0 & \Theta\theta & 0 & -\Theta\theta \\ 0 & 0 & 0 & 0 \\ 0 & -\Theta\theta & 0 & \Theta\theta \end{bmatrix}}_{\Gamma} \underbrace{\begin{bmatrix} W(0) \\ \Phi(0) \\ W(L) \\ \Phi(L) \end{bmatrix}}_{d}.
\tag{40}
$$

Combining equations (32) and (40), we can relate the nodal displacements and forces by considering the piezoelectric effect:

$$f = \underbrace{\left(HR^{-1} + \Gamma\right)}_{D(\omega)} d. \tag{41}$$

$D(\omega)$ in the above equation is the spectral element matrix of the piezoelectric metamaterial beam. For a piezoelectric metamaterial beam that consists of multiple segments, we can construct the global dynamic stiffness matrix by assembling all the spectral elements of those segments. Note that in a piezoelectric metamaterial beam, the piezoelectric material does not necessarily cover the entire beam. For beam segments without piezoelectric coverage, their dynamic stiffness matrices can be readily obtained by omitting the electromechanical coupling terms in $D(\omega)$ in equation (41). When constructing the global dynamic stiffness matrix of a general piezoelectric metamaterial beam, it is essential to consider both types of dynamic stiffness matrices during the matrix assembling process.

2.4. Implementation of boundary conditions

After obtaining the dynamic stiffness matrix of a single segment or the global structure, we impose the boundary conditions on the derived set of equations to investigate the dynamics of the piezoelectric metamaterial beam from different aspects.

2.4.1. Floquet boundary condition. To derive the dispersion relation of the piezoelectric metamaterial beam, we take a representative unit cell, i.e. a single segment, and apply the Floquet periodic boundary condition [69]. First, we convert the dynamic stiffness matrix into the transfer matrix:

$$T(\omega) = \begin{bmatrix} -D_{LR}^{-1}D_{LL} & -D_{LR}^{-1} \\ D_{RL} - D_{RR}D_{LR}^{-1}D_{LL} & -D_{RR}D_{LR}^{-1} \end{bmatrix} \tag{42}$$

where D_{LL}, D_{LR}, D_{RL}, and D_{RR} are the four D_{LL} quadrants of the dynamic stiffness matrix $D(\omega)$. They follow the below relationship:

$$D(\omega) = \begin{bmatrix} D_{LL} & D_{LR} \\ D_{RL} & D_{RR} \end{bmatrix}. \tag{43}$$

The transfer matrix (equation (42)) relates the dynamics of the two nodes of a segment in the below manner:

$$\begin{bmatrix} W(0) \\ \Phi(0) \\ -Q(0) \\ -M(0) \end{bmatrix} = \underbrace{\begin{bmatrix} -D_{LR}^{-1}D_{LL} & -D_{LR}^{-1} \\ D_{RL} - D_{RR}D_{LR}^{-1}D_{LL} & -D_{RR}D_{LR}^{-1} \end{bmatrix}}_{T(\omega)} \begin{bmatrix} W(L) \\ \Phi(L) \\ Q(L) \\ M(L) \end{bmatrix}. \tag{44}$$

On the other hand, the Floquet periodic boundary condition requires

$$\begin{bmatrix} W(0) \\ \Phi(0) \\ -Q(0) \\ -M(0) \end{bmatrix} = e^{iqL} \underbrace{\begin{bmatrix} 1 & 0 & 0 & 0 \\ 0 & 1 & 0 & 0 \\ 0 & 0 & 1 & 0 \\ 0 & 0 & 0 & 1 \end{bmatrix}}_{I} \begin{bmatrix} W(L) \\ \Phi(L) \\ Q(L) \\ M(L) \end{bmatrix} \tag{45}$$

where q is the wavenumber. Comparing equations (44) and (45), we obtain a standard eigenvalue problem:

$$\left| T(\omega) - e^{iqL}I \right| = 0. \tag{46}$$

For a given ω, we can solve equation (46) to derive the corresponding wavenumber q. By plotting ω versus q, we can sketch the band structure of the piezoelectric metamaterial beam. Based on the characteristics of the solution of q, i.e. whether q is real or imaginary, we know the wave of the corresponding frequency is a propagating or evanescent wave. In the diagram showing only the real part of q versus ω, the blank areas without any real solutions of q denote the band gaps. The above analysis applies to a single segment with two nodes. However, according to the structural geometry, a representative unit cell may contain multiple segments. In view of this situation, we can condense the internal nodes. We first rewrite equation (41) as

$$\begin{bmatrix} f_L \\ f_I \\ f_R \end{bmatrix} = \begin{bmatrix} D_{LL} & D_{LI} & D_{LR} \\ D_{IL} & D_{II} & D_{IR} \\ D_{RL} & D_{RI} & D_{RR} \end{bmatrix} \begin{bmatrix} d_L \\ d_I \\ d_R \end{bmatrix} \tag{47}$$

where the subscripts *L, I*, and *R* denote the left end, the internal, and the right end nodes, respectively; $d_L = \begin{bmatrix} W_{\mathrm{lhs}} & \Phi_{\mathrm{lhs}} \end{bmatrix}^T$ and $d_R = \begin{bmatrix} W_{\mathrm{rhs}} & \Phi_{\mathrm{rhs}} \end{bmatrix}^T$. Note that the Floquet periodic condition is only applied at the boundaries, i.e. the two end nodes, and the internal nodes are not constrained, which implies $f_I = 0$; thus, d_I can be eliminated, and equation (47) can be reduced to a simpler form as

$$\begin{bmatrix} f_L \\ f_R \end{bmatrix} = \underbrace{\begin{bmatrix} D_{LL} - D_{LI}D_{II}^{-1}D_{IL} & D_{LR} - D_{LI}D_{II}^{-1}D_{IR} \\ D_{RL} - D_{RI}D_{II}^{-1}D_{IL} & D_{RR} - D_{RI}D_{II}^{-1}D_{IR} \end{bmatrix}}_{D_{\mathrm{Cond}}(\omega)} \begin{bmatrix} d_L \\ d_R \end{bmatrix}. \tag{48}$$

After dynamic condensation, we can treat $D_{\mathrm{Cond}}(\omega)$ as that of a single segment. Therefore, the above procedures can be applied to obtain the transfer matrix of the condensed dynamic stiffness matrix, and then derive the dispersion relation.

2.4.2. Clamped-free boundary condition. In the above dispersion relation analysis, the piezoelectric metamaterial beam is assumed to be infinitely long. However, any practical system has a finite length. Therefore, the transmittance of a finitely long model is also an important figure of merit for evaluating the actual vibration suppression performance. In this paper, we

compute the transmittance of a finitely long model under the clamped-free boundary condition. The left end of the piezoelectric metamaterial beam is fixed to a clamper that is mounted on a shaker. The left end can be subjected to a force or pre-described displacement, but the rotation of the left end is constrained to be zero. In the first case, we consider a unit force is applied to the left end of the model. The governing equation can be expressed as:

$$
\boldsymbol{D}_{\text{global}}
\begin{bmatrix}
W_{\text{lhs}} \\
\Phi_{\text{lhs}} = 0 \\
\vdots \\
W_{\text{rhs}} \\
\Phi_{\text{rhs}}
\end{bmatrix}
=
\begin{bmatrix}
1 \\
0 \\
\vdots \\
0 \\
0
\end{bmatrix}.
\tag{49}
$$

Note that the boundary condition requires $\Phi_{\text{lhs}} = 0$, the second row and the second column of the global dynamic stiffness matrix $\boldsymbol{D}_{\text{global}}$ can be directly crossed out

$$
\begin{bmatrix}
D_{11} & \cancel{D_{12}} & \cdots & D_{1n} \\
\cancel{D_{21}} & \cancel{D_{22}} & \cancel{\times} & \cancel{D_{2n}} \\
\vdots & \cancel{\vdots} & \ddots & \vdots \\
D_{n1} & \cancel{D_{n2}} & \cdots & D_{nn}
\end{bmatrix}
\begin{bmatrix}
W_{lhs} \\
0 \\
\vdots \\
W_{rhs} \\
\Phi_{rhs}
\end{bmatrix}
=
\begin{bmatrix}
1 \\
0 \\
\vdots \\
0 \\
0
\end{bmatrix}
\tag{50}
$$

Solving equation (50) yields the solutions of the nodal displacements, i.e. $W_{\text{lhs}}\ldots$, W_{rhs} and Φ_{rhs}. The transmittance of the piezoelectric metamaterial beam can be obtained as:

$$
T = 20\log_{10}\left(\frac{|W_{\text{rhs}}|}{|W_{\text{lhs}}|}\right).
\tag{51}
$$

In the second case, we can apply a unit transverse displacement to the left end of the model. Thereby, the governing equation can be written as:

$$
\boldsymbol{D}_{\text{global}}
\begin{bmatrix}
W_{\text{lhs}} = 1 \\
\Phi_{\text{lhs}} = 0 \\
\vdots \\
W_{\text{rhs}} \\
\Phi_{\text{rhs}}
\end{bmatrix}
=
\begin{bmatrix}
Q_{\text{lhs}} \\
M_{\text{lhs}} \\
\vdots \\
0 \\
0
\end{bmatrix}.
\tag{52}
$$

By rearranging equation (52) to make the unknown parameters appear on the left-hand side, we obtain:

$$
\begin{bmatrix}
-\boldsymbol{I} & \boldsymbol{D}_{(1..2,\,3..n)} \\
\boldsymbol{0} & \boldsymbol{D}_{(3..n,\,3..n)}
\end{bmatrix}
\begin{bmatrix}
Q_{lhs} \\
M_{lhs} \\
\vdots \\
W_{rhs} \\
\Phi_{rhs}
\end{bmatrix}
=
\begin{bmatrix}
1 \\
0 \\
\vdots \\
0 \\
0
\end{bmatrix}
\tag{53}
$$

where $\boldsymbol{D}_{(a..b,\,c..d)}$ denotes the submatrix by taking the block of the entries ranging from ath to bth row and cth column

to dth column in the global dynamic stiffness matrix $\boldsymbol{D}_{\text{global}}$. Equation (53) becomes easily solvable. Based on the solutions of (53), the transmittance of the piezoelectric metamaterial beam can then be computed as:

$$
T = 20\log_{10}\left(|W_{\text{rhs}}|\right).
\tag{54}
$$

In fact, equation (54) gives the same result as that calculated by equation (51).

3. Verification case studies

In this section, several case studies are presented, and corresponding FE models are built for comparison to verify the theoretical method developed in section 2. The multi-physics FE software COMSOL is used for carrying out the verification. In COMSOL, we built the corresponding models using the 'Solid Mechanics' module and 2D plane-stress simulation.

3.1. Uniform configuration in parallel connection

The first case study considers a piezoelectric metamaterial beam that is fully covered by the piezoelectric layer, as shown in figure 1. The top and bottom piezoelectric layers in each unit cell are connected in parallel, as shown in figure 2(a), then shunted to the external inductive circuit, as shown in figure 3(a). The inductance of the inductor used in this case study is about 1.242 H, which is intended to make the LC resonant frequency of a unit cell, i.e. $1/\left(2\pi\sqrt{L_I C_p}\right)$, 800 Hz. It is referred to as the uniform configuration in parallel connection for brevity. The material and geometric parameters of this in-parallel configuration are listed in table 1.

Figure 4 presents the band structure of the piezoelectric metamaterial beam configured with in parallel connection. The solid black curve denotes the solution of the model established using the SEM. The red circles represent the COMSOL result. It is worth noting that by using the solid mechanics module of COMSOL, we can only sweep the wavenumber and then solve the eigenfrequency. Thus, the COMSOL simulation result only contains the real part of the wavenumber. That is why figure 4(b) does not include the corresponding COMSOL result. The SEM is superior from this point of view, but this does not mean that the FE method is entirely at a loss in terms of seeking the imaginary part of the wavenumber. Using the extended wave FE method (WFEM) [70] or constructing a numerical model using the partial differential equations (PDEs) module in COMSOL [71] are two feasible ways to seek the imaginary solution of the wavenumber. However, additional mathematical treatments and post-processing operations must be introduced if one wants to employ the WFEM or the PDE method. In addition, the WFEM method and the PDE module in FE software rely on spatial discretization and suffer from convergence issues. High-frequency and high-precision analyses often require extensive mesh refinement, making numerical methods computationally inefficient. In contrast, the SEM method presented in this work is an analytical method. It provides rigorous and exact solutions

Table 1. Material and geometric parameters of the piezoelectric metamaterial beam.

Substrate layer—Brass			
Mass density ρ_s	7165 kg m^{-3}	Young's modulus E_s	100 GPa
Shear modulus G_s	40 Gpa	Substrate width b	10 mm
Substrate thickness h_s	0.5 mm	Substrate length l_s	40 mm

Piezoelectric layer—PZT-5			
Mass density ρ_p	7800 kg m^{-3}	Young's modulus $C_{11}{}^E$	66 GPa
Shear modulus $C_{55}{}^E$	21 GPa	Substrate width b	10 mm
Substrate thickness h_p	0.4 mm	Substrate length l_p	40 mm
Piezoelectric permittivity $\varepsilon_{33}{}^T$	15.93 nF m^{-1}	Piezoelectric constant e_{31}	-12.54 C m^{-2}

Figure 4. The band structure of the configuration in parallel connection with the LC resonant frequency of 800 Hz: (a) the real part and (b) the imaginary part of the wavenumber solution. The black curves are SEM results, and the red circles are COMSOL simulation results. The orange and cerulean strips, respectively, indicate the LR- and BS-type band gaps.

with lower computational costs. The analytical nature eliminates the need for excessive mesh refinement while maintaining computational efficiency.

After a digression for interested readers and to avoid any misunderstanding, let us get back to the topic of this study. From figure 4(a), we can see that the SEM result matches perfectly well with the COMSOL result. Two band gaps, denoted by the colour-shaded areas in figure 4(a), occur in the band structure plot. The first band gap forms over the frequency range from 728.4 to 795.4 Hz, with the upper bound around the designed LR resonant frequency of 800 Hz. According to the theories in the existing literature [44, 72], we can speculate the first band gap should be the LR mechanism-induced band gap, which is referred to as the LR-type band gap hereinafter. On the other hand, we can determine whether a band gap is formed due to the LR or the BS mechanism by inspecting the imaginary part evolution in the band gap region [73]. A sharp spike appears in the imaginary part of the first band gap region, as shown in figure 4(b). This observation has been widely reported for many LR metamaterials. While in the second band gap that is formed at a higher frequency from 1008 to 1202 Hz, the imaginary part varies much more smoothly, which is typical behaviour of BS-type band gaps. The imaginary part of the wavenumber is also an indicator of the attenuation property in the band gap region. Comparing the magnitudes of the imaginary part in the two band gaps, we can predict that

the band gap will exhibit a much stronger vibration attenuation ability, while the vibration attenuation region corresponding to the second band gap in a practical system may be inappreciable [32].

In addition to the band structure analysis, the transmittance of a finitely long model that consists of six unit cells is also investigated. The system parameters are the same as listed in table 1. Complex moduli are introduced to consider the damping effect in materials. In all the following calculations and simulations of transmittances, the loss factor is set to be $\zeta = 0.016$. To be more specific, the Young's moduli of the substrate material and the piezoelectric material become $E_c(1 + i\zeta)$ and $C_{11}^E(1 + i\zeta)$, respectively. This is equivalent to setting the damping ratio around the structural resonance to 0.008, which is around the common values of many engineering materials. Figure 5(a) compares the transmittances calculated by the SEM and obtained by the FE simulation. It can be seen that both results are in good agreement over the spectrum under investigation. Just below 800 Hz, a vibration attenuation region appears that corresponds to the first band gap predicted by the band structure analysis in figure 4(a). Moreover, as predicted by the imaginary part of the wavenumber (figure 4(b)), the attenuation capability of the second band gap is too weak, thus, its corresponding vibration attenuation region is imperceptible on the transmittance curve. Figure 5(b) shows the enlarged view of
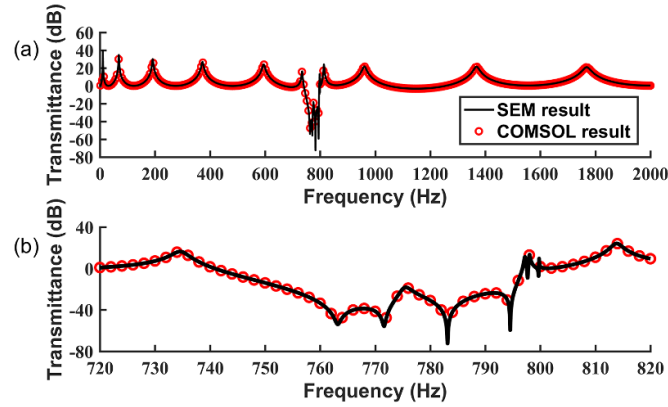
Figure 5. (a) The transmittance of the piezoelectric metamaterial beam consisting of six unit cells that are configured in parallel connection and with the LC resonant frequency of 800 Hz. (b) The enlarged view of the vibration attenuation region.
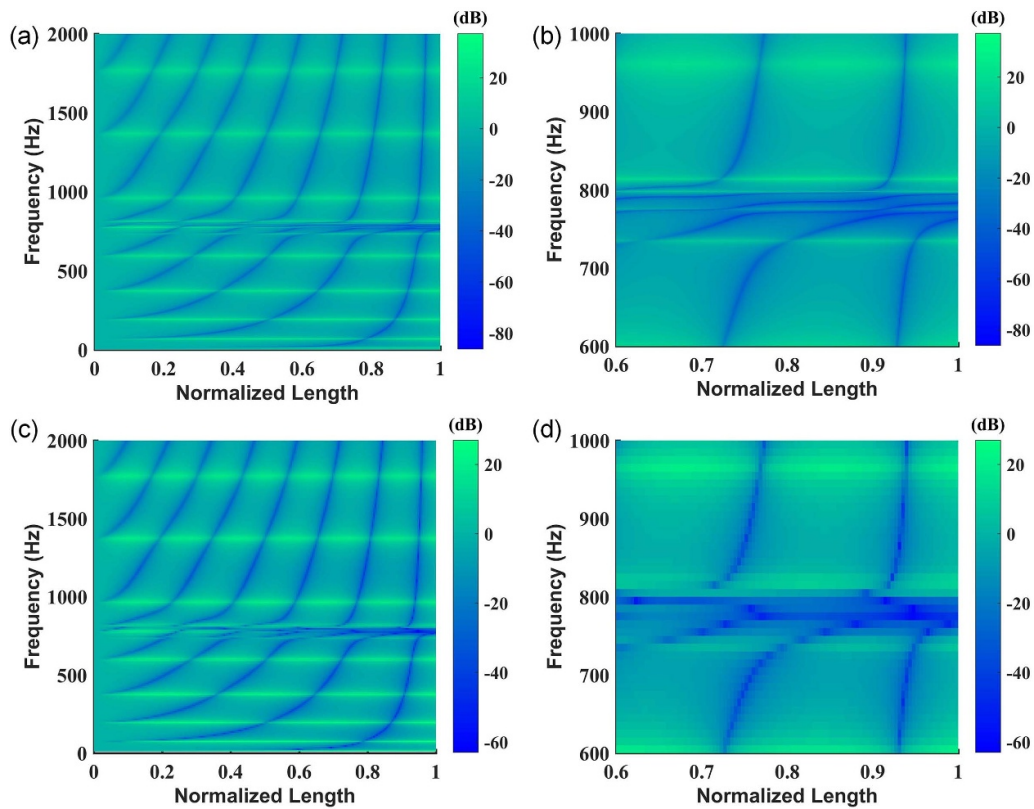

Figure 6. The transmittance contour showing the dependence on the frequency and beam location: (a) the SEM result; (b) the enlarged view of the SEM result; (c) the COMSOL result; (d) the enlarged view of the COMSOL result. The blue and green colours indicate weak and intense vibrations, respectively. The spectral element method is much computationally efficient, and the enlarged view in figure (b) provides more details than in figure (d).

the vibration attenuation region in figure 5(a). It is observed that those red circles (COMSOL result) tightly stick to the black curve (SEM result). The high accuracy of the SEM is further verified by the delicate comparison in figure 5(b).

In section 2 when deriving the mathematical formulation, each unit cell was treated as a two-node segment, the displacement field information was concealed. In fact, the displacement field along the beam can be easily retrieved by making use of the relationship between the node displacements and the displacement field, i.e. equation (30). To demonstrate

the versatility of the SEM, the transmittance contour that contains all the information along the whole metamaterial beam and over the entire spectrum is plotted in figure 6(a). The COMSOL result is also provided in figure 6(c) for comparison. One cannot find any big difference after a quick glance over figures 6(a) and (c), which means the SEM result coincides with the COMSOL result well. In fact, the SEM is much more efficient, at least in our case. By using the SEM, we can easily reduce the sweep steps to obtain a higher-resolution contour plot. The enlarged views presented in figures 6(b)
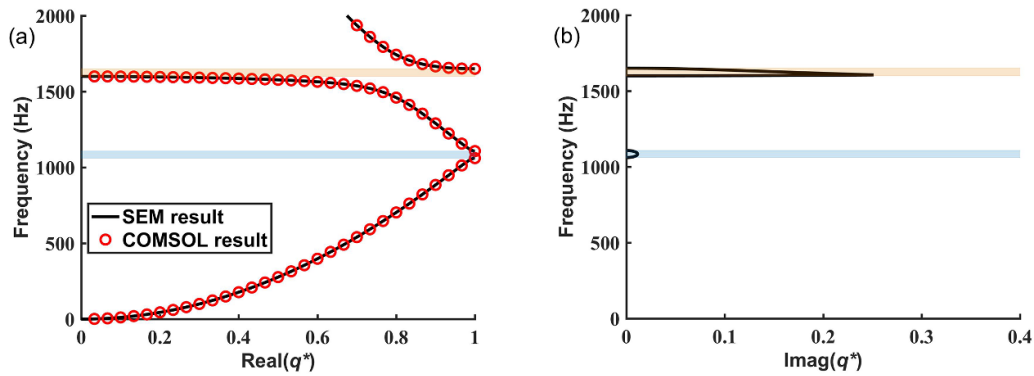
Figure 7. The band structure of the configuration in series connection with the shunted inductor of 1.242 H, i.e. the LC resonant frequency of 1600 Hz: (a) the real part and (b) the imaginary part of the wavenumber solution. The black curves are SEM results, and the red circles are COMSOL simulation results. The orange and cerulean strips, respectively, indicate the LR- and BS-type band gaps.

and (d) show that the details contained in the SEM result are much more refined, even though the COMSOL simulation took much longer time to produce figure 6(b).

3.2. Uniform configuration in series connection

As aforementioned, the two piezoelectric layers in each unit cell can be connected in either parallel or series. The second case study considers a model with the same parameters listed in table 1 but implemented in the series connection. If we adaptively change the inductance of the inductor to 4.969 H to make the LC resonant frequency of a unit cell, i.e. $1/\left(2\pi\sqrt{L_I C_p}\right)$, still be 800 Hz, the band structure and transmittance of the in-series configuration are completely the same as those of the in-parallel configuration presented in section 3.1. Thus, the results are not presented to avoid duplication. Instead of fixing the LC resonant frequency, we remain the inductor unchanged in the following study, which implies the LC resonant frequency, i.e. $1/\left(2\pi\sqrt{L_I C_p}\right)$, will increase by two times to 1600 Hz.

Figure 7 presents the band structure of the piezoelectric metamaterial beam with the two piezoelectric layers in the unit cell connected in series. Unsurprisingly, the SEM result is in good consistency with the COMSOL result. It is found that a band gap forms from 1600 to 1650 Hz. As the LC resonant frequency is just 1600 Hz, it can be inferred that this band gap is quite possibly induced by the LR mechanism. In addition to the LR-type band gap, there appears another band gap below it, ranging from 1061 to 1108 Hz. To further ascertain the band gap type, we can survey the imaginary part of the wavenumber, as illustrated in figure 7(b). Since the magnitude of the imaginary part varies smoothly in the first band gap, while shows up a spike in the second band gap, we can confirm that the first and second band gaps belong to the BS-type and LR-type, respectively. This result reveals that the conclusion in [44], i.e. the LC resonant frequency is the upper bound of the piezoelectric metamaterial beam, is not always valid. According to the study of [8], the band gap edge estimation formulas derived by the modal method in [44] are only applicable within the
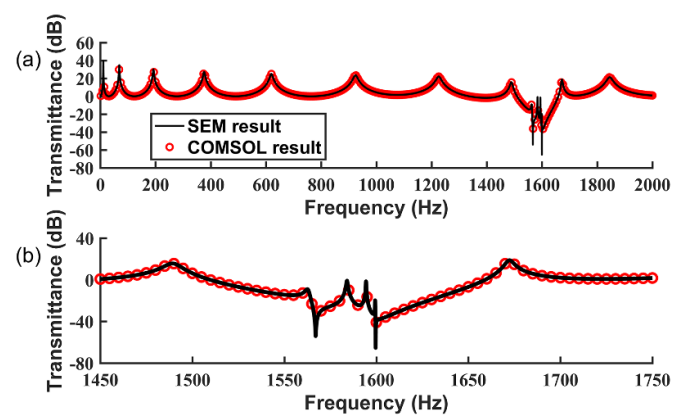

Figure 8. (a) The transmittance of the piezoelectric metamaterial beam consisting of 6 unit cells that are configured in series connection and with the shunted inductor of 1.242 H, i.e. the LC resonant frequency of 1600 Hz. (b) The enlarged view of the vibration attenuation region.

non-deep-subwavelength regions. The last point that is worth mentioning is, similar to the result of the in-parallel configuration, the result of the band structure analysis for the in-series configuration also predicts that the attenuation capability of the BS-type band gap is much weaker than that of the LR-type one.

Subsequently, the transmittance of a finitely long model that consists of 6 unit cells is investigated. The SEM and COMSOL results are plotted in figure 8(a). As expected, both results match with each other well. The transmittance result also agrees with the prediction of the band structure analysis: (1) a vibration attenuation region is formed around 1600 Hz, which is the LC resonant frequency; (2) the BS-type band gap fails to generate a noticeable vibration attenuation region on the transmittance curve. Figure 8(b) presents the enlarged view of the vibration attenuation region. Even after zooming in, the difference between the SEM and COMSOL results is still negligible, which firmly proves the high accuracy of the SEM.
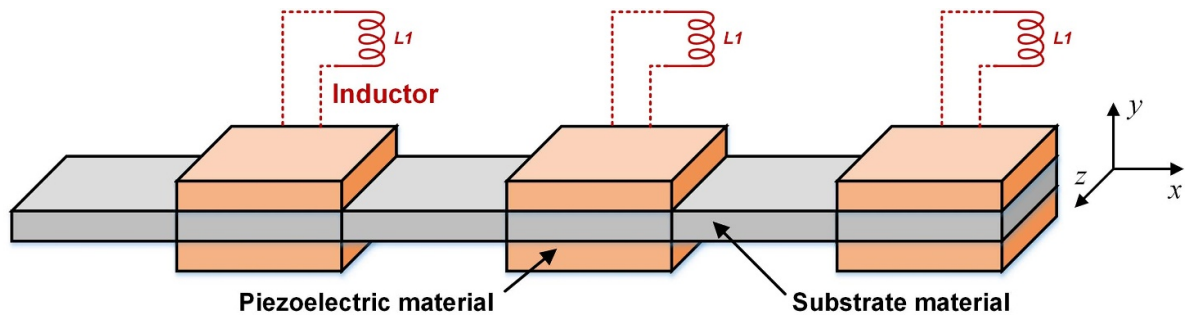
Figure 9. Schematic of a uniform piezoelectric metamaterial beam with periodic spacing between the piezoelectric layers along the beam length direction.

3.3. Stepped configuration with periodic spacing

The adjacent unit cells of the piezoelectric metamaterial shown in figure 1 are electrically insulated and separated but still physically unbroken. That model represents a theoretical design that is difficult to realize since the electrode implementation is not easy, and the adopted long piezoelectric patch will be fragile. This subsection demonstrates the versatility of the SEM method by using it to model a more practical design, as shown in figure 9.

Stocky and less fragile piezoelectric patches are periodically bonded on the substrate beam. As the piezoelectric patches are spatially spaced, electrical insulation treatment is not required anymore. The piezoelectric patches in each unit cell are configured in parallel connection. The material and geometric parameters of this configuration are still the same as those listed in table 1, except for the piezoelectric patch length. The substrate length of a unit cell is still 40 mm. The length of each piezoelectric patch is 20 mm. Similar models have ever been studied in [74–76] using the TMM method and based on the Euler–Bernoulli theory. Figure 10 presents the band structure result of the piezoelectric metamaterial beam with periodic spacing. The results obtained by COMSOL and the TMM method [74–76] are also provided for comparison. Due to the existence of periodic spacing, mechanical impedance mismatching, i.e. thickness difference & bending stiffness contrast, between neighbouring segments becomes significant. Hence, multiple evident Bragg band gaps, as can be observed in figure 10(a), are produced over a broad frequency range of 0–8000 Hz. From the profile of the imaginary part illustrated in figure 10(b), we can identify that the second band gap should belong to the LR-type as it appears like a sharp spike. Figures 10(c) and (d) show the enlarged view around the first two band gaps over the frequency range of 0–2000 Hz. Moreover, figures 10(c) and (d) show the enlarged view around the first two band gaps over the frequency range of 6000–8000 Hz. Still, the SEM result agrees with the COMSOL simulation result, especially in the low-frequency range. Slight discrepancies are noticed in the high-frequency range. A discussion will be presented in section 4.1 to explain the high-frequency discrepancies.

For the TMM method used in [74–76], the results also overlap with the SEM and COMSOL results in this low-frequency range, as shown in figures 10(c) and (d). However, when the frequency increases, significant discrepancies arise in the TMM results, as observed in figures 10(e) and (f). The fourth band gap spans over [6084, 7355] Hz, according to the COMSOL result. The predictions by the TMM and SEM methods are, respectively, [6305, 7477] Hz and [6204, 7360] Hz. When comparing the upper bounds, the TMM exhibits an error of 1.659%, while the SEM shows a much lower error of 0.068%. This highlights the improved accuracy achieved by the SEM method, along with the utilization of Timoshenko's beam theory, in predicting high-frequency results. In addition to band structures, transmittance plots are presented in figure 11. The finitely long model for generating the transmittance plots consists of 6 unit cells. One can effortlessly find three vibration attenuation valleys over the transmittance curve shown in figure 11(a). The depths of the vibration attenuation valleys are consistent with the predictions by the attenuation factors, i.e. the imaginary part of wavenumbers, as manifested in figure 10(b). The first band gap failed to produce a conspicuous attenuation valley since it is narrow in bandwidth and weak in attenuation strength. Figures 11(b) and (c) present the enlarged views of the transmittance curve around the LR band gap region around 800 Hz and the second Bragg band gap region around 2000–4000 Hz. As already learned from the band structure results presented in figure 10, the transmittance results in figure 11 also confirm the excellent agreement between the SEM and COMSOL results in the low-frequency range. However, the SEM curve marginally drifts away from the COMSOL one in the high-frequency range.

For the TMM method used in [74–76], the corresponding results shown in figure 11(b) match the COMSOL and SEM ones only in the low-frequency range. However, upon closer examination of the enlarged view in figure 11(b), noticeable discrepancies persist between the TMM result and the COMSOL and SEM results. More importantly, a critical instability issue occurs in the numerical solution of the TMM method over the high-frequency range beyond 2200 Hz. This instability renders the TMM result meaningless, as demonstrated in the enlarged view displayed in figure 11(c). This numerical instability constitutes a significant drawback of the standard/classical TMM method [77, 78]. Especially for large-scale structures, such as the piezoelectric metamaterial beam consisting of multiple cells, the TMM method involves the successive multiplication of transfer matrices (as illustrated in figure 12(a)). This process accumulates round-off
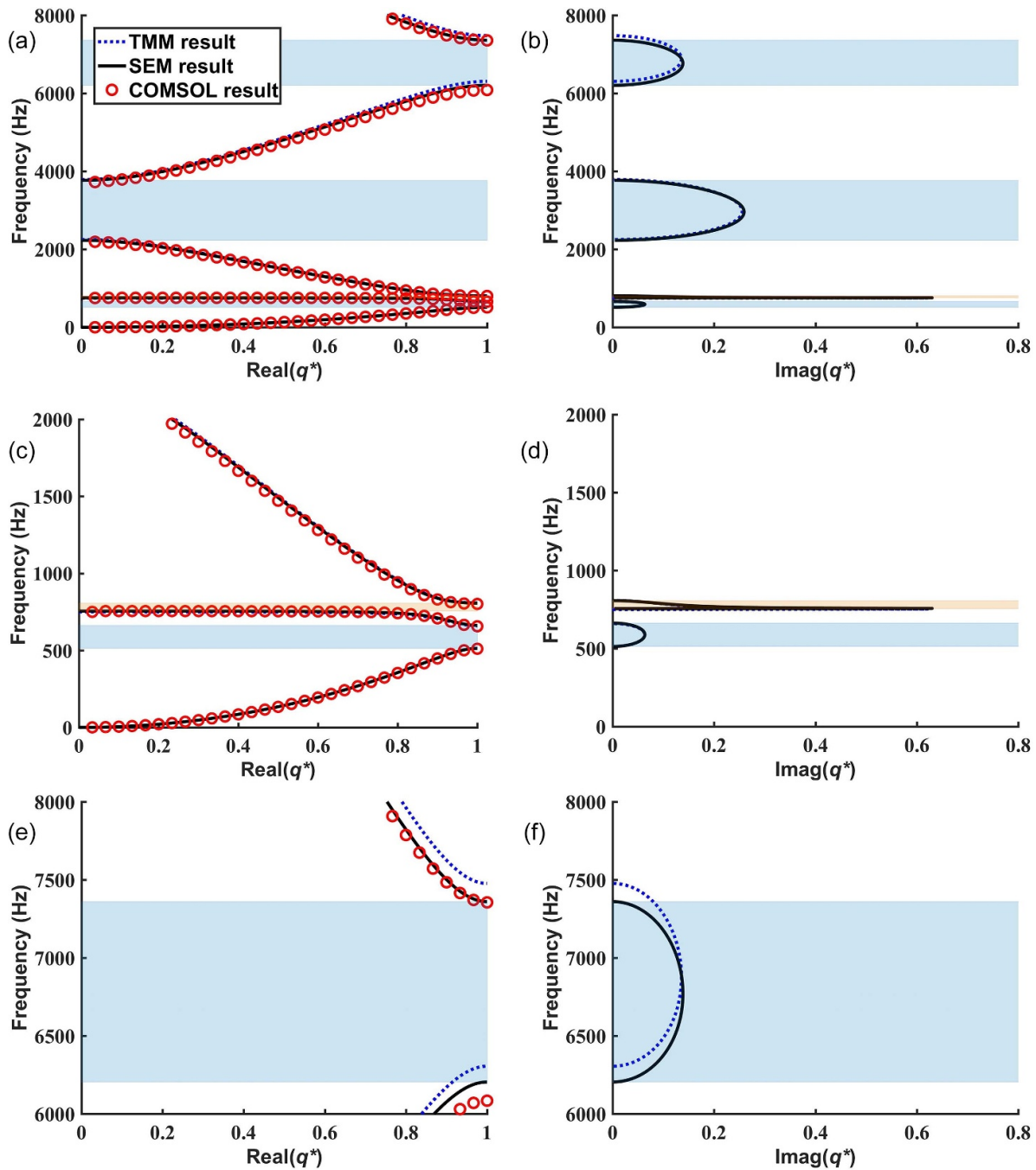
Figure 10. The band structure of the piezoelectric metamaterial beam with periodic uniform gaps, the LC resonant frequency set to 800 Hz: (a) the real part; (b) the imaginary part. The enlarged view of the band structure over the frequency range of 0–2000 Hz: (c) the real part; (d) the imaginary part. The enlarged view of the band structure over the frequency range of 6000–8000 Hz: (e) the real part; (f) the imaginary part. The black curves represent the SEM results, and the red circles are the COMSOL simulation results. The orange and cerulean strips, respectively, indicate the LR- and BS-type band gaps.

errors, leading to an ill-conditioned and extremely stiff global transfer matrix as the frequency increases. Unlike the TMM method, the SEM method assembles the global dynamic stiffness matrix in a summative manner, as graphically depicted in figure 12(b). In this approach, round-off errors do not multiply as in the TMM method. Therefore, the SEM method demonstrates significantly improved robustness and stability compared to the TMM method.

The above observations highlight the limitations of the TMM method, including the persistent discrepancies with COMSOL and SEM results and the critical numerical instability that arises at higher frequencies. Conversely, the SEM method offers enhanced reliability and stability due to its summative assembly of the global dynamic stiffness matrix, making it a preferable choice for analysing large-scale structures such as piezoelectric metamaterial beams.
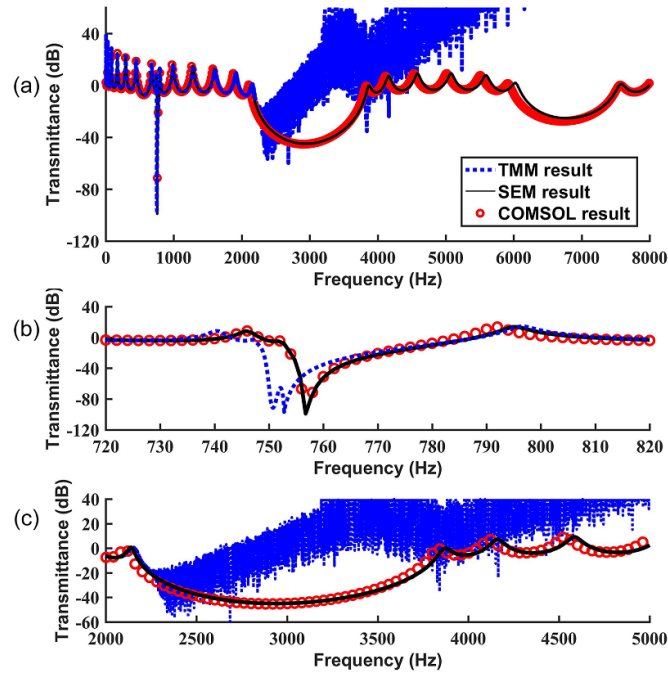
Figure 11. (a) The transmittance of the piezoelectric metamaterial beam consisting of 6 unit cells with periodic spacing and configured in parallel connection, with the LC resonant frequency set to 800 Hz. The enlarged view of the vibration attenuation region over the frequency range of: (b) 720–820 Hz, and (c) 2000–5000 Hz.
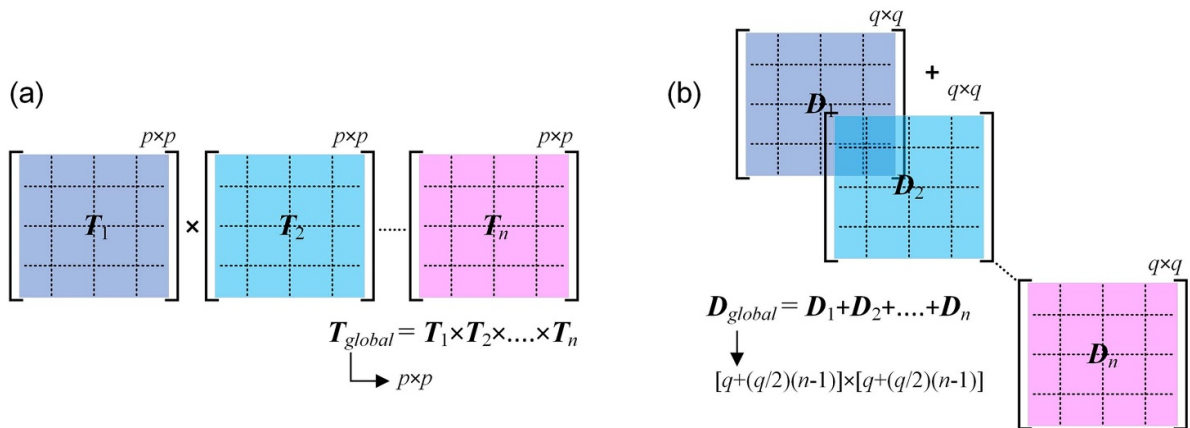

Figure 12. Graphical demonstration of constructing (a) the global transfer matrix in the TMM method; and (b) the global dynamic stiffness matrix in the SEM method.

3.4. Stepped configuration with length grading

The piezoelectric metamaterial beams in previous sections all follow periodic patterns. In recent years, removing periodicity and introducing grading strategies in designing metamaterials have attracted lots of research interest [79, 80]. From the geometric and structural perspective, metamaterials designed in grading patterns are usually more complicated, thus imposing more difficulties in developing their models. Following the study and model in [81], this subsection demonstrates how to use the SEM method to model a piezoelectric metamaterial beam with length grading, as shown in figure 13.

It is referred to as the stepped configuration with length grading hereafter. The length of the first cell is still 40 mm. The piezoelectric coverage ratio in each cell is always 50%. It implies the piezoelectric patch length in the first cell is 20 mm. From left to right, the cell length reduces, and the piezoelectric patch gets shorter as well. A grading factor δ is defined as follows:

$$\delta_g = \frac{1}{n}\left(1 - \frac{l_{n+1}}{l_1}\right) = 0.05. \tag{55}$$

Strictly speaking, the structure cannot be deemed as metamaterial after removing the periodicity. Therefore,
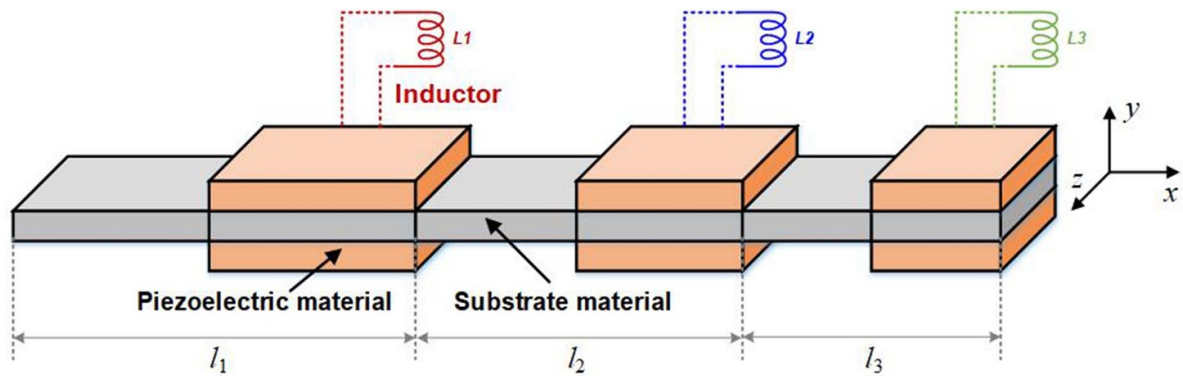
Figure 13. Schematic of a piezoelectric metamaterial beam with grading piezoelectric patches. Note that the length of the segment decreases from the left to the right. The internal capacitance of the piezoelectric element accordingly varies, thus, the shunted inductance is adjusted to ensure the LC resonant frequency is kept the same.
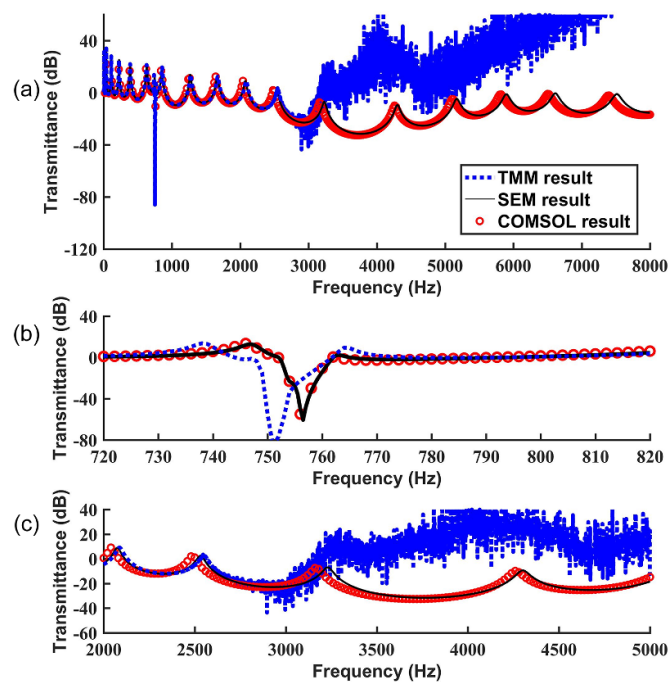

Figure 14. (a) The transmittance of the piezoelectric metamaterial beam consisting of 6 unit cells with length grading, the LC resonant frequencies are all set to 800 Hz. The enlarged view of the vibration attenuation region over the frequency range: (b) 720–820 Hz, and (c) 2000–5000 Hz.

examining the transmittance curve to find out the attenuation valleys is a more direct and reliable way to evaluate the vibration attenuation performance. Figure 14(a) presents the transmittance result of the stepped configuration with length grading over the frequency range of 0–8000 Hz. Figures 14(b) and (c) present the enlarged views over 720–820 Hz and 2000–5000 Hz, respectively. Overall, we can say that the SEM result matches the COMSOL. At the same time, we must admit that the discrepancy in the high-frequency range becomes visible to the naked eye. We also used the TMM method to calculate the transmittance of this model in the way as in [81]. The TMM method shows less accuracy than the SEM method in the low-frequency range and exhibits numerical instability when the frequency exceeds 2600 Hz. Back to the result itself, comparing figure 14(b) with figure 13(b), we

can find that the LR-induced vibration attenuation valley of the stepped configuration with length grading becomes narrower. This is because the grading strategy is implemented only in cell length but not the electrical parameters. The LR resonant frequencies are all set to 800 Hz. As the piezoelectric patches holistically get shorter, circuit resonance produced counteraction bending moments become weaker. Thus, the LR-induced vibration attenuation valley becomes smaller.

Comparing figure 14(c) with figure 13(c), we can observe that the BS-induced vibration attenuation valley becomes much broader, starting from almost 2000 Hz and going up beyond 5000 Hz. This broadband effect can be explained by reminiscing the BS mechanism. It is known that Bragg band gaps depend on lattice constants. As the lattice constant decreases, the corresponding Bragg band gap tends to form in
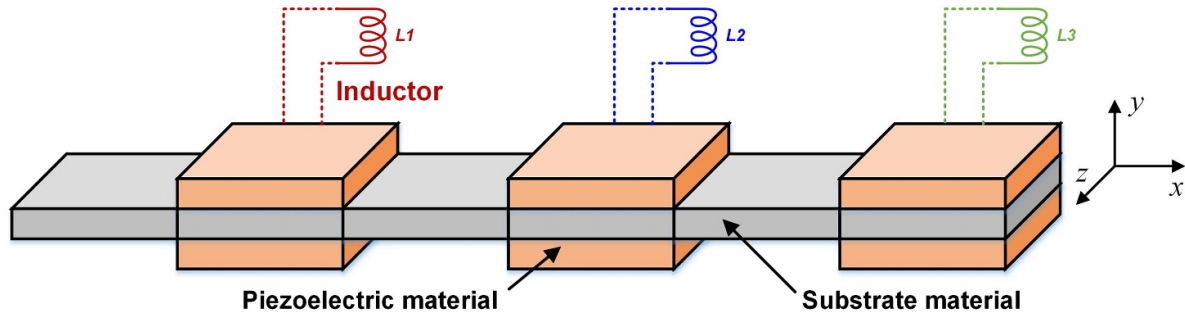
Figure 15. Schematic of a piezoelectric metamaterial beam with geometric uniformity but circuit (inductor) grading. The inductance of the inductor shunted to the piezoelectric segment increases from the left to the right. Thus, the LC resonant frequency increases accordingly.

a higher frequency range. In the stepped configuration with length grading, the cell length gets smaller from the left to the right-hand side. Therefore, the BS phenomenon occurs over different frequency ranges in different cells. As these frequency ranges overlap, there forms a broad attenuation region. However, the attenuation region widening is at the sacrifice of the attenuation strength, i.e. the valley becomes much shallower.

3.5. Stepped configuration with inductor grading

In addition to geometric parameters, grading strategies can also be adopted in designing circuit parameters of piezoelectric metamaterials [48, 82]. By virtue of assembly procedures, the SEM method can also be used to model piezoelectric metamaterials with circuit grading conveniently. This subsection considers an example case, as demonstrated in figure 15. The geometric structure of this configuration is the same as the previous one that is shown in figure 9. The LC resonant frequencies of the piezoelectric cells from left to right are labelled as f_1, f_2, … The grading factor, in this case, is defined as:

$$\delta_c = \frac{1}{n}\left(\frac{f_{n+1}}{f_1} - 1\right) = 0.05 \tag{56}$$

where $f_1 = 800$ Hz. The example case considers a model consisting of 6 cells. The sequent LC resonant frequencies gradually increase and are 840, 880, 920, 960, and 1000 Hz, respectively.

Similarly, the transmittance of this configuration is calculated to assess its vibration attenuation performance. Note that the required inductances to achieve those LC resonant frequencies are much larger than common values. Hence, we usually use synthetic circuits [83] to simulate those inductors for constituting the shunt circuits of piezoelectric metamaterials. Parasitic resistances unavoidably exist in synthetic circuits due to the non-idealities of the practical op-amps [84]. Figures 16(a) and (b) present the results of the ideal situation when there does not exist any parasitic resistance and the practical situation with a parasitic resistance of 300 Ω.

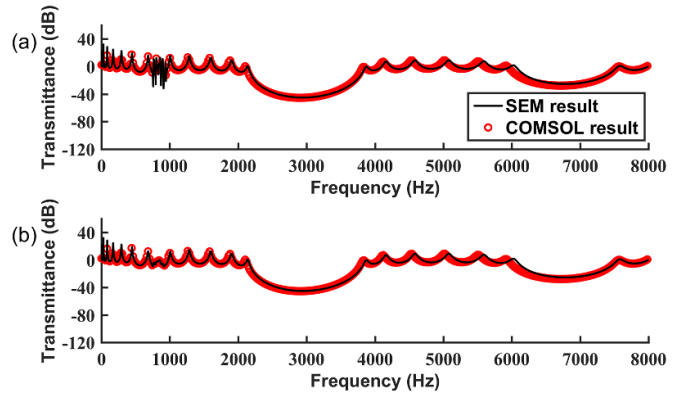Again, the SEM method well predicts the transmittance profiles. Compared with figure 11(a), it can be seen that the

Figure 16. The transmittance of the stepped configuration with inductor grading. The model consists of 6 cells, the LC resonant frequencies are set to 800, 840, 880, 920, 960, and 1000 Hz, respectively. (a) The parasitic resistance of the shunt circuit is 0 Ω; (b) The parasitic resistance of the shunt circuit is 300 Ω.

shallow attenuation valleys in the relatively high-frequency range are almost unaffected. This is because they are formed by the BS mechanism, which mainly depends on the lattice constant. Since the geometric periodicity is kept untouched, the BS-type attenuation valleys remain nearly unchanged. However, there is a dramatic change in the LR-type attenuation valley: the downward spike in the deep valley disappears, and that fraction curve becomes rather rippled, spreading over a broad frequency range. Figure 17 presents the enlarged view around the LR-type attenuation valley. Compared with figure 11(b), the single deep valley is split into pieces, i.e. totally 6 smaller valleys with shallower depths. Each small and shallow valley corresponds to each LR resonance. From the width perspective, the 6 small valleys, as a whole, spread over a broader frequency range. However, those small peaks between the 6 valleys are undesired for vibration attenuation. If parasitic resistances exist in the synthetic circuits, those small peaks can be flattened and suppressed below 0 dB. Unfortunately, the consequence is that the depths of the valleys become further shallower. Therefore, the existence of parasitic resistances only benefits broadband vibration attenuation but weakens the attenuation strengths.
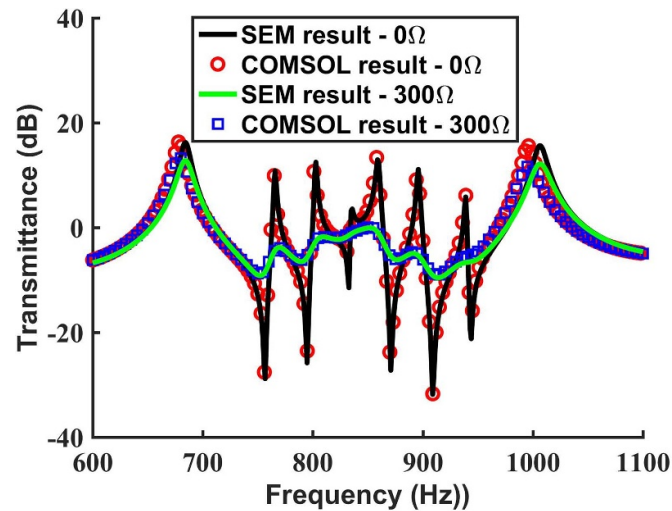
Figure 17. Enlarged view of the transmittance of the stepped configuration with inductor grading over the LR-induced attenuation region. With the increase of the parasitic resistance in the shunt circuit, the valleys and peaks within the band gap region become significantly flattened, while the outside peaks only slightly decrease.
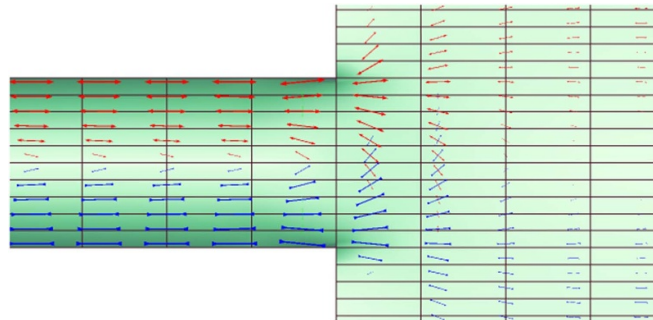

Figure 18. Stress distribution around the place where the cross-section abruptly changes. The contour colour indicates the stress magnitude, and the arrows denote the principal stress directions. Stress concentration appears at the acute angled corners of the intersection.
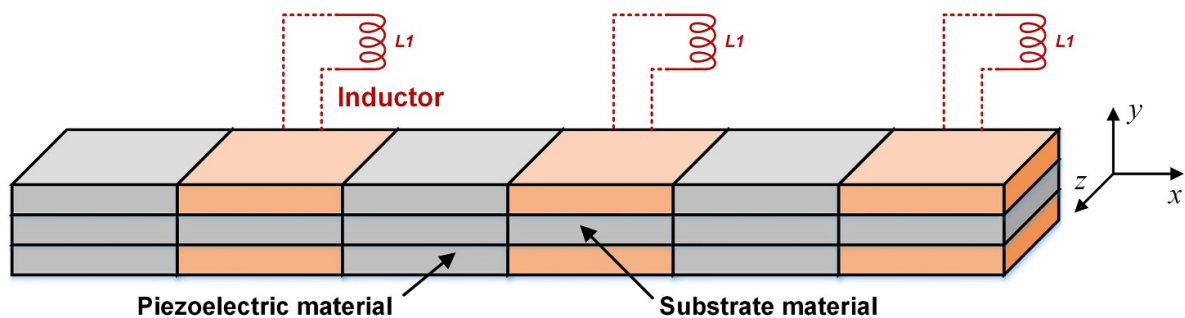

Figure 19. Schematic of a thickness-uniform piezoelectric metamaterial beam with piezoelectric patches periodically embedded in the substrate material. The top and bottom surfaces of the whole beam are flat.

4. Further discussion

A number of case studies presented in section 3 have verified the versatility of the SEM method. In most cases, the SEM results can precisely match the simulated ones. However, the accuracy slightly reduces as the frequency increases. The following section 4.1 discusses the reason for causing the high-frequency discrepancy. What is the necessity of developing high-accuracy models for piezoelectric metamaterials?

Section 4.2 will present a study based on the SEM model for merging LR and Bragg band gaps, which exemplifies the usefulness of the proposed method.

4.1. Cause of model accuracy degradation

One may have noticed that the SEM method consistently exhibits high accuracy in dealing with uniform configurations. Noticeable discrepancies appear in predicting the
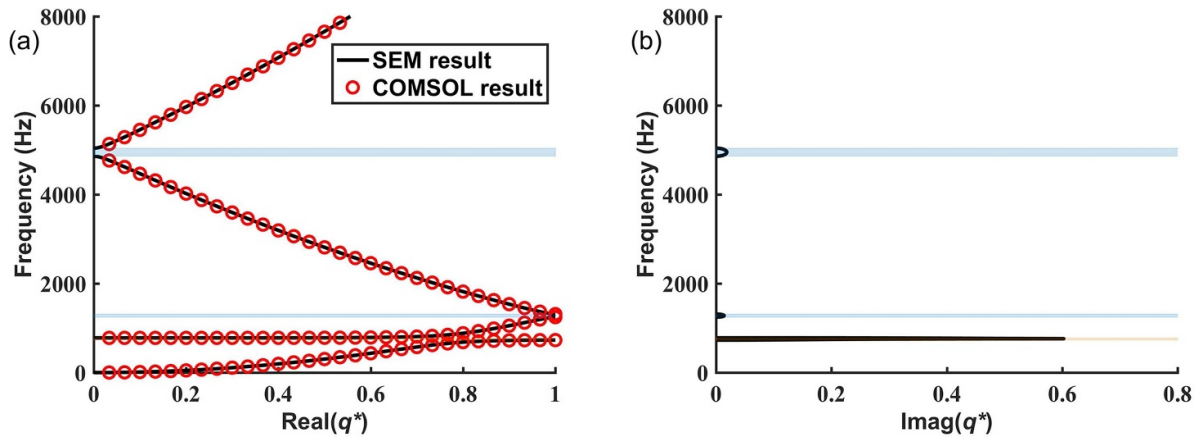
Figure 20. The band structure of the additional configuration, the LC resonant frequency is set to 800 Hz: (a) the real part and (b) the imaginary part of the wavenumber solution. The black curves are SEM results, and the red circles are COMSOL simulation results. The orange and cerulean strips, respectively, indicate the LR- and BS-type band gaps.
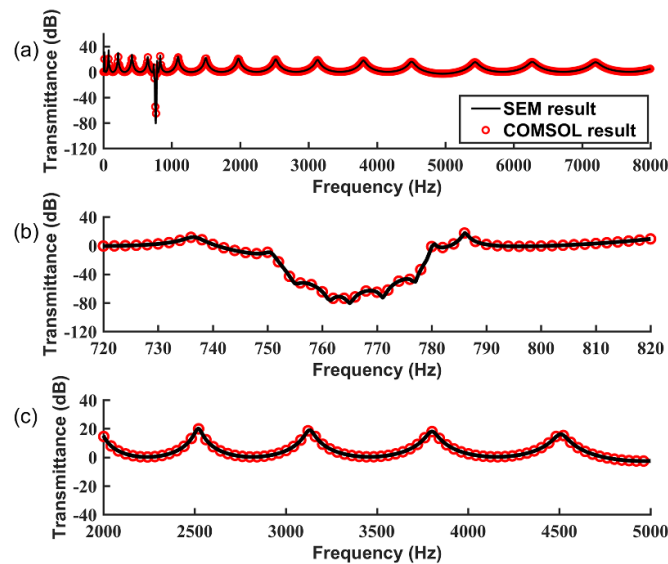

Figure 21. (a) The transmittance of the addition configuration consisting of 6 cells, the LC resonant frequency is set to 800 Hz. The enlarged view of the vibration attenuation region over the frequency range: (b) 720–820 Hz, and (c) 2000–5000 Hz.

high-frequency responses of the stepped ones. It can thus be easily deduced that the errors are attributed to the stepped feature, i.e. the abrupt change in cross-section. When the beam is under bending deformation, stress distribution around the stepped interface becomes irregular, and stress concentration occurs, as shown in figure 18. The stress concentration effect causes local deformation and reduces the bending stiffness at the joint connection [85]. In other words, applying Timoshenko's beam theory without considering the stress concentration effect leads to overestimating the bending stiffness at the abruptly changed cross-section. That is why those peaks in the high-frequency ranges of figures 11, 13, and 15 predicted by the SEM method are in close proximity to those simulated ones but at their right-hand sides.

To further prove that the discrepancies are originated from the stepped feature in the geometry, an additional configuration, as shown in figure 19, is considered. In this configuration, the piezoelectric patches are periodically embedded into the substrate material without affecting the beam thickness, thus, the beam is geometrically flat. The geometric and material parameters are the same as those of the configuration presented in figure 11 in section 3.3. The parallel connection strategy is applied for implementing the circuits of this configuration.

Figure 20 presents the band structure of this additional configuration. It can be seen that even though the piezoelectric patches are still distributed periodically with a certain distance between each other, as in those stepped configurations, the analytically computed dispersion curve can excellently match the simulation results with an imperceptible difference in the high-frequency range.

In addition to the band structure, transmittance curves are compared in figure 21. Almost zero discrepancy is observed by naked eyes in the enlarged views over both the low- and high-frequency ranges. The red circles that represent the simulation results stick tightly to the black curve obtained
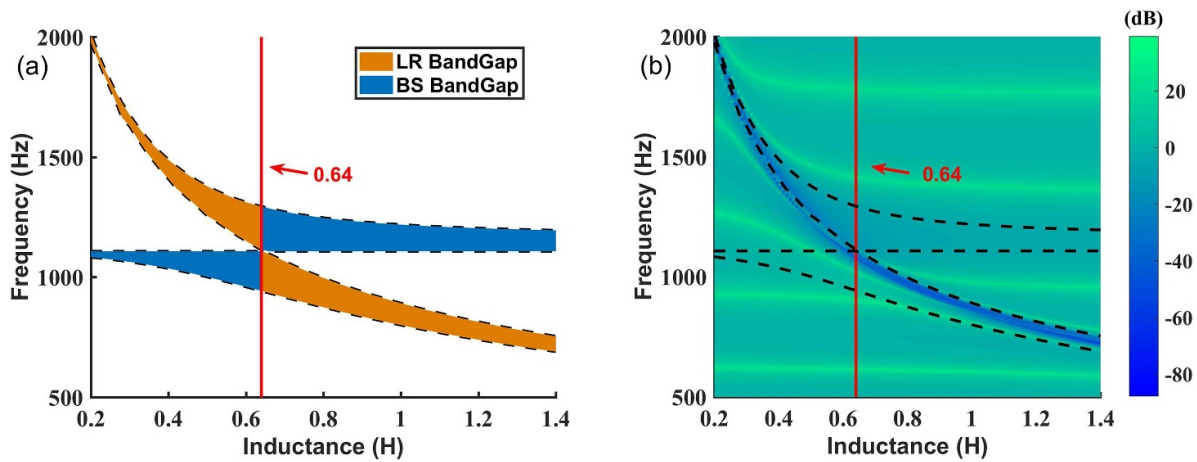
Figure 22. (a) Effect of inductance on the band gap formation; (b) effect of inductance on the transmittance profile for the model consisting of 6 cells. The positions of the LR and BS band gaps swap after the inductance crossing 0.64 H. The LR and BS band gaps almost overlap with each other when the inductance reach the critical value 0.64 H.
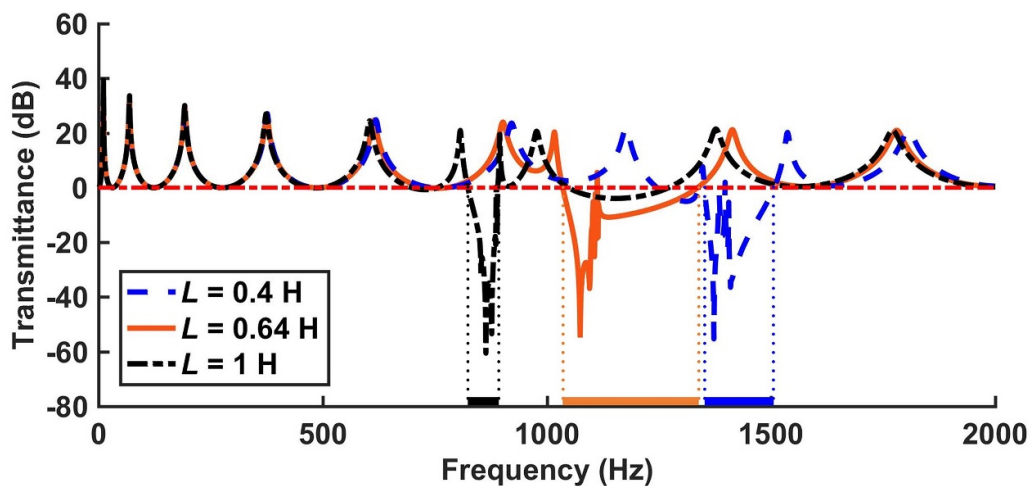

Figure 23. Comparison of the transmittance profiles of three cases with different inductances. The coloured heavy horizontal lines near the bottom of the abscissa denote the attenuation region widths. The attenuation region of the case with $L = 0.64$ H (in the orange colour) is the widest.

by the SEM method. According to the above analysis and comparison studies, it can now be firmly confirmed that the stepped feature in geometry is responsible for the model accuracy degradation. Further refining the model by taking account of the stress concentration effect around the abruptly changed beam cross-section could be a meaningful prospective study.

4.2. Merging band gaps towards optimization

Though using commercial FE software can also simulate the dynamic responses and foresee the band gap behaviour of piezoelectric metamaterials, the analytical models developed based on the SEM method are much more computationally efficient. Therefore, we can carry out optimizations based on the analytical models. This section presents a parametric-based optimization case study for demonstration. The results

presented in this section are all obtained by the analytical model based on the SEM method.

From the two case studies presented in sections 3.1 and 3.2, one may have already noted that by changing the inductance, the LR-type band gap could appear below (figure 4) or above (figure 7) the first BS-type band gap. Therefore, we wonder whether it is possible to couple the LR- and BS-type band gaps by selecting an appropriate inductance. To answer this question, we first performed a parametric study to investigate the effect of the inductance on the band gap formation of the piezoelectric metamaterial studied in section 3.1. Figure 22(a) reveals how the band gap regions evolve in response to the inductance change. Blue and orange shaded areas, respectively, denote the BS and LR band gaps. The BS-type band gap always forms around 1100 Hz since the lattice constant is unchanged regardless of the change in the inductance. The LR-type band gap moves down as the inductance increases since the LR resonant frequency increases with the inductance.

When the inductance is tuned around 0.64 H, the widths of both the LR- and BS-type band gaps attain the maximum, and they overlap with each other, forming a coupled wide band gap.

Figure 22(b) illustrates the transmittance variation of the piezoelectric metamaterial beam in the contour form. As indicated by the colour bar, dark blue denotes small transmittance, and light green signifies large transmittance. The dashed curves are the borderlines of the band gaps extracted from figure 22(a). The transmittance results conform to the band structure prediction: the dark blue areas are within the dashed borderlines, indicating vibration attenuation regions. The colour within the dashed borderlines of the BS-type band gap is not in dark blue but also not in light green since the attenuation strength is weak.

Three typical inductance values are selected. One is 0.64 Hz, the optimal case identified in figure 22(a). The other two values are, respectively, picked from the two sides of the optimal point. The transmittances of their corresponding cases are compared in figure 23. The coloured heavy horizontal lines near the bottom of the abscissa denote the attenuation region widths. The band gaps of the three cases, i.e. $L = 0.4$ H, 0.64 H, and 1 H, are 823.6–890.4 Hz, 1035.2–1335.9 Hz, and 1351.4–1506.7 Hz, respectively. As compared to the two normal cases, i.e. $L = 0.4$ H and 1 H, the band gap width of the optimal one, i.e. $L = 0.64$ H, has been widened by 350.1% and 93.6%, respectively. This case study shows that after optimization based on the analytical model, the vibration attenuation performance of the piezoelectric metamaterial beam can be significantly enhanced from the broadband perspective.

5. Conclusion

In this paper, we have presented a high-accuracy and universal modelling approach for piezoelectric metamaterial beams. The governing equations have been obtained based on the constitutive equations of materials and using Hamilton's principle. The dynamic stiffness matrix of a general composite piezoelectric beam segment shunted to any inductive and resistive circuit has been derived. Implementation of the boundary conditions for conducting band structure and transmittance analyses has been demonstrated. Five case studies of piezoelectric metamaterial beams in different configurations have been presented to prove the versatility of the proposed approach. Two configurations have a constant beam cross-section but with different electrode connections. The other three configurations have stepped beam cross-sections. Length and electrical parameters grading strategies have been, respectively, introduced in two of them. Compared to their FE models, the high accuracy of the theoretical models developed using the refined modelling approach has been verified. Only minor discrepancies exist in predicting the high-frequency responses of stepped configurations. A further discussion has explained the reason for the accuracy degradation. Since the

stress concentration effect caused by the sudden changes in beam cross-sections is not considered in the modelling, the theoretical model overestimates the bending stiffness of the beam at those joint connections. Finally, the value of the proposed approach has been reflected by a parametric-based optimization study for merging the BS and LR band gaps in an example piezoelectric metamaterial beam to form a coupled wide band gap.

Data availability statement

The data cannot be made publicly available upon publication because they are not available in a format that is sufficiently accessible or reusable by other researchers. The data that support the findings of this study are available upon reasonable request from the authors.

Conflict of interest

The authors declare that they have no known competing financial interests or personal relationships that could have appeared to influence the work reported in this paper.

ORCID iDs

Guobiao Hu ⓘ https://orcid.org/0000-0002-1288-7564
Lihua Tang ⓘ https://orcid.org/0000-0001-9031-4190
Yaowen Yang ⓘ https://orcid.org/0000-0002-7856-2009

References

[1] Hussein M I, Leamy M J and Ruzzene M 2014 Dynamics of phononic materials and structures: historical origins, recent progress, and future outlook *Appl. Mech. Rev.* **66** 040802
[2] Lim C 2021 From photonic crystals to seismic metamaterials: a review via phononic crystals and acoustic metamaterials *Arch. Comput. Methods Eng.* **29** 1137–98
[3] Deymier P A 2013 *Acoustic Metamaterials and Phononic Crystals* vol 173 (Springer)
[4] Fang S, Zhou S, Yurchenko D, Yang T and Liao W-H 2022 Multistability phenomenon in signal processing, energy harvesting, composite structures, and metamaterials: a review *Mech. Syst. Signal Process.* **166** 108419
[5] Muhammad, Zhou W and Lim C 2019 Topological edge modeling and localization of protected interface modes in 1D phononic crystals for longitudinal and bending elastic waves *Int. J. Mech. Sci.* **159** 359–72
[6] Liu Z Y, Zhang X X, Mao Y W, Zhu Y Y, Yang Z Y, Chan C T and Sheng P 2000 Locally resonant sonic materials *Science* **289** 1734–6

[7] Yu D, Liu Y, Wang G, Zhao H and Qiu J 2006 Flexural vibration band gaps in Timoshenko beams with locally resonant structures *J. Appl. Phys.* **100** 124901

[8] Xiao Y, Wang S, Li Y and Wen J 2021 Closed-form bandgap design formulas for beam-type metastructures *Mech. Syst. Signal Process.* **159** 107777

[9] Wen S, Xiong Y, Hao S, Li F and Zhang C 2020 Enhanced band-gap properties of an acoustic metamaterial beam with periodically variable cross-sections *Int. J. Mech. Sci.* **166** 105229

[10] Chang I-L, Liang Z-X, Kao H-W, Chang S-H and Yang C-Y 2018 The wave attenuation mechanism of the periodic local resonant metamaterial *J. Sound Vib.* **412** 349–59

[11] Mei C, Li L, Tang H, Han X, Wang X and Hu Y 2021 Broadening band gaps of shear horizontal waves of metamaterials via graded hierarchical architectures *Compos. Struct.* **271** 114118

[12] Huang G and Sun C 2010 Band gaps in a multiresonator acoustic metamaterial *J. Vib. Acoust.-Trans. ASME* **132** 031003

[13] Hu G, Tang L, Das R, Gao S and Liu H 2017 Acoustic metamaterials with coupled local resonators for broadband vibration suppression *AIP Adv.* **7** 025211

[14] Zhu R, Liu X, Hu G, Sun C and Huang G 2014 A chiral elastic metamaterial beam for broadband vibration suppression *J. Sound Vib.* **333** 2759–73

[15] Fang X, Wen J, Bonello B, Yin J and Yu D 2017 Ultra-low and ultra-broad-band nonlinear acoustic metamaterials *Nat. Commun.* **8** 1288

[16] Bae M H and Oh J H 2022 Nonlinear elastic metamaterial for tunable bandgap at quasi-static frequency *Mech. Syst. Signal Process.* **170** 108832

[17] Tan K T, Huang H H and Sun C T 2012 Optimizing the band gap of effective mass negativity in acoustic metamaterials *Appl. Phys. Lett.* **101** 241902

[18] Chen H, Li X, Chen Y and Huang G 2017 Wave propagation and absorption of sandwich beams containing interior dissipative multi-resonators *Ultrasonics* **76** 99–108

[19] Li Q, He Z and Li E 2019 Dissipative multi-resonator acoustic metamaterials for impact force mitigation and collision energy absorption *Acta Mech.* **230** 2905–35

[20] Lu K, Wu J H, Jing L and Guan D 2017 Flexural vibration bandgaps in local resonance beam with a novel two-degree-of-freedom local resonance system *Eur. Phys. J. Appl. Phys.* **77** 20501

[21] Li Z, Hu H and Wang X 2018 A new two-dimensional elastic metamaterial system with multiple local resonances *Int. J. Mech. Sci.* **149** 273–84

[22] Khajehtourian R and Hussein M 2014 Dispersion characteristics of a nonlinear elastic metamaterial *AIP Adv.* **4** 124308

[23] Fang X, Wen J, Yin J and Yu D 2016 Wave propagation in nonlinear metamaterial multi-atomic chains based on homotopy method *AIP Adv.* **6** 121706

[24] Hu G, Tang L and Das R 2018 Internally coupled metamaterial beam for simultaneous vibration suppression and low frequency energy harvesting *J. Appl. Phys.* **123** 055107

[25] Lu K, Wu J H, Jing L, Gao N and Guan D 2017 The two-degree-of-freedom local resonance elastic metamaterial plate with broadband low-frequency bandgaps *J. Phys. D: Appl. Phys.* **50** 095104

[26] Yu D, Liu Y, Zhao H, Wang G and Qiu J 2006 Flexural vibration band gaps in Euler-Bernoulli beams with locally resonant structures with two degrees of freedom *Phys. Rev. B* **73** 064301

[27] Terao T 2016 Wave propagation in acoustic metamaterial double-barrier structures *Phys. Status Solidi* a **213** 2773–9

[28] Meng Z, Wang L, Li Z and Wang J 2023 A theoretical framework for joining multiple locally resonant bandgaps

of metamaterials towards a super-wide bandgap *Compos. Struct.* **304** 116348

[29] Thorp O, Ruzzene M and Baz A 2001 Attenuation and localization of wave propagation in rods with periodic shunted piezoelectric patches *Smart Mater. Struct.* **10** 979

[30] Casadei F, Delpero T, Bergamini A, Ermanni P and Ruzzene M 2012 Piezoelectric resonator arrays for tunable acoustic waveguides and metamaterials *J. Appl. Phys.* **112** 064902

[31] Xu J and Tang J 2017 Tunable prism based on piezoelectric metamaterial for acoustic beam steering *Appl. Phys. Lett.* **110** 181902

[32] Hu G, Xu J, Tang L, Lan C and Das R 2019 Tunable metamaterial beam using negative capacitor for local resonators coupling *J. Intell. Mater. Syst. Struct.* **31** 389–407

[33] Liu Y, Wang H, Fang W, Han Q, Liu D and Liang Y 2021 Tunable control of subwavelength topological interface modes in locally resonance piezoelectric metamaterials *Compos. Struct.* **276** 114541

[34] Ren T, Li F, Chen Y, Liu C and Zhang C 2020 Improvement of the band-gap characteristics of active composite laminate metamaterial plates *Compos. Struct.* **254** 112831

[35] Gripp J and Rade D 2018 Vibration and noise control using shunted piezoelectric transducers: a review *Mech. Syst. Signal Process.* **112** 359–83

[36] De Marneffe B and Preumont A 2008 Vibration damping with negative capacitance shunts: theory and experiment *Smart Mater. Struct.* **17** 035015

[37] Wang Y-F, Wang Y-Z, Wu B, Chen W and Wang Y-S 2020 Tunable and active phononic crystals and metamaterials *Appl. Mech. Rev.* **72** 040801

[38] Chen Y, Huang G and Sun C 2014 Band gap control in an active elastic metamaterial with negative capacitance piezoelectric shunting *J. Vib. Acoust.* **136** 061008

[39] Zhu R, Chen Y Y, Barnhart M V, Hu G K, Sun C T and Huang G L 2016 Experimental study of an adaptive elastic metamaterial controlled by electric circuits *Appl. Phys. Lett.* **108** 011905

[40] Chen S, Wen J, Wang G, Yu D and Wen X 2012 Improved modeling of rods with periodic arrays of shunted piezoelectric patches *J. Intell. Mater. Syst. Struct.* **23** 1613–21

[41] Chen S, Wen J, Yu D, Wang G and Wen X 2011 Band gap control of phononic beam with negative capacitance piezoelectric shunt *Chin. Phys.* B **20** 014301

[42] Yi K and Collet M 2021 Broadening low-frequency bandgaps in locally resonant piezoelectric metamaterials by negative capacitance *J. Sound Vib.* **493** 115837

[43] Wang X, Wang L, Shu H and Zhang L 2022 Research on dual-functional properties of an improved piezoelectric metamaterial beam for simultaneous vibration suppression and energy harvesting *Appl. Phys.* A **128** 1–19

[44] Sugino C, Leadenham S, Ruzzene M and Erturk A 2017 An investigation of electroelastic bandgap formation in locally resonant piezoelectric metastructures *Smart Mater. Struct.* **26** 055029

[45] Bao B, Lallart M and Guyomar D 2020 Manipulating elastic waves through piezoelectric metamaterial with nonlinear electrical switched dual-connected topologies *Int. J. Mech. Sci.* **172** 105423

[46] Zheng Y, Zhang J, Qu Y and Meng G 2022 Investigations of a piezoelectric metastructure using negative-resistance circuits to enhance the bandgap performance *J. Vib. Control* **28** 2346–56

[47] Xu J, Lu H, Qin W, Wang P and Bian J 2022 Mechanical shunt resonators-based piezoelectric metamaterial for elastic wave attenuation *Materials* **15** 891

[48] Jian Y, Tang L, Hu G, Li Z and Aw K C 2022 Design of graded piezoelectric metamaterial beam with spatial variation of electrodes *Int. J. Mech. Sci.* **218** 107068

[49] Lin Z, Al Ba'ba'a H and Tol S 2021 Piezoelectric metastructures for simultaneous broadband energy harvesting and vibration suppression of traveling waves *Smart Mater. Struct.* **30** 075037

[50] Sugino C, Ruzzene M and Erturk A 2017 Dynamics of hybrid mechanical-electromechanical locally resonant piezoelectric metastructures *ASME 2017 Conf. on Smart Materials, Adaptive Structures and Intelligent Systems* (American Society of Mechanical Engineers) (https://doi.org/10.1115/SMASIS2017-3948)

[51] Zhou W, Wu Y and Zuo L 2015 Vibration and wave propagation attenuation for metamaterials by periodic piezoelectric arrays with high-order resonant circuit shunts *Smart Mater. Struct.* **24** 065021

[52] Rao S S and Yap F F 2011 *Mechanical Vibrations* vol 4 (Prentice hall Upper Saddle River)

[53] Lee U and Kim J 2000 Dynamics of elastic-piezoelectric two-layer beams using spectral element method *Int. J. Solids Struct.* **37** 4403–17

[54] Park I and Lee U 2012 Dynamic analysis of smart composite beams by using the frequency-domain spectral element method *J. Mech. Sci. Technol.* **26** 2511–21

[55] Lee U, Kim D and Park I 2013 Dynamic modeling and analysis of the PZT-bonded composite Timoshenko beams: spectral element method *J. Sound Vib.* **332** 1585–609

[56] Wang G 2013 Analysis of bimorph piezoelectric beam energy harvesters using Timoshenko and Euler–Bernoulli beam theory *J. Intell. Mater. Syst. Struct.* **24** 226–39

[57] Li F-M and Liu C-C 2015 Vibration analysis and active control for frame structures with piezoelectric rods using spectral element method *Arch. Appl. Mech.* **85** 675–90

[58] Wu Z-J, Li F-M and Zhang C 2014 Vibration properties of piezoelectric square lattice structures *Mech. Res. Commun.* **62** 123–31

[59] Jang I, Park I and Lee U 2014 Guided waves in a Timoshenko beam with a bonded composite patch: frequency domain spectral element modeling and analysis *Composites* B **60** 248–60

[60] Abad F and Rouzegar J 2019 Exact wave propagation analysis of moderately thick Levy-type plate with piezoelectric layers using spectral element method *Thin-Walled Struct.* **141** 319–31

[61] Ren T, Liu C, Li F and Zhang C 2020 Active tuning of the vibration band gap characteristics of periodic laminated composite metamaterial beams *J. Intell. Mater. Syst. Struct.* **31** 843–59

[62] Fiborek P, Soman R, Kudela P and Ostachowicz W 2022 Spectral element modeling of ultrasonic guided wave propagation in optical fibers *Ultrasonics* **124** 106746

[63] Alan S and Bediz B 2021 A novel electromechanical spectral element method for piezoelectric energy harvester plates *J. Sound Vib.* **505** 116139

[64] Machado M R, Fabro A T and de Moura B B 2020 Spectral element approach for flexural waves control in smart material beam with single and multiple resonant impedance shunt circuit *J. Comput. Nonlinear Dyn.* **15** 121003

[65] Shen Y, Zhang P, He W, Xu M and Duan Q 2021 Transverse vibration responses of the in-plane-wise functionally graded piezoelectric composite plates *Mech. Adv. Mater. Struct.* **30** 592–608

[66] Ji H, Qiu J, Cheng J and Inman D 2011 Application of a negative capacitance circuit in synchronized switch damping techniques for vibration suppression *J. Vib. Acoust.* **133** 041015

[67] 1996 IEEE Standard on piezoelectricity *IEEE Trans. Ultrason. Ferroelectr. Freq. Control* **43** A1–54

[68] Song Y, Kim S, Park I and Lee U 2015 Dynamics of two-layer smart composite Timoshenko beams: frequency domain spectral element analysis *Thin-Walled Struct.* **89** 84–92

[69] Åberg M and Gudmundson P 1997 The usage of standard finite element codes for computation of dispersion relations in materials with periodic microstructure *J. Acoust. Soc. Am.* **102** 2007–13

[70] Yang Y, Kingan M J and Mace B R 2022 Analysis of the forced response of coupled panels using a hybrid finite element/wave and finite element method *J. Sound Vib.* **537** 117174

[71] Zhou W, Wu B, Chen Z, Chen W, Lim C and Reddy J 2020 Actively controllable topological phase transition in homogeneous piezoelectric rod system *J. Mech. Phys. Solids* **137** 103824

[72] Jian Y, Hu G, Tang L, Xu J and Aw K C 2021 A generic theoretical approach for estimating bandgap bounds of metamaterial beams *J. Appl. Phys.* **130** 054501

[73] Xiao Y, Wen J, Yu D and Wen X 2013 Flexural wave propagation in beams with periodically attached vibration absorbers: band-gap behavior and band formation mechanisms *J. Sound Vib.* **332** 867–93

[74] Hao Z, Ji-Hong W, Sheng-Bing C, Gang W and Xi-Sen W 2015 Flexural wave band-gaps in phononic metamaterial beam with hybrid shunting circuits *Chin. Phys.* B **24** 036201

[75] Airoldi L and Ruzzene M 2011 Design of tunable acoustic metamaterials through periodic arrays of resonant shunted piezos *New J. Phys.* **13** 113010

[76] Wang G, Wang J, Chen S and Wen J 2011 Vibration attenuations induced by periodic arrays of piezoelectric patches connected by enhanced resonant shunting circuits *Smart Mater. Struct.* **20** 125019

[77] Rong B, Lu K, Ni X and Ge J 2020 Hybrid finite element transfer matrix method and its parallel solution for fast calculation of large-scale structural eigenproblem *Appl. Math. Modelling* **77** 169–81

[78] Dazel O, Groby J-P, Brouard B and Potel C 2013 A stable method to model the acoustic response of multilayered structures *J. Appl. Phys.* **113** 083506

[79] Hu G, Austin A C, Sorokin V and Tang L 2021 Metamaterial beam with graded local resonators for broadband vibration suppression *Mech. Syst. Signal Process.* **146** 106982

[80] De Ponti J M, Colombi A, Riva E, Ardito R, Braghin F, Corigliano A and Craster R V 2020 Experimental investigation of amplification, via a mechanical delay-line, in a rainbow-based metamaterial for energy harvesting *Appl. Phys. Lett.* **117** 143902

[81] Jian Y, Hu G, Tang L, Tang W, Abdi M and Aw K C 2023 Analytical and experimental study of a metamaterial beam with grading piezoelectric transducers for vibration attenuation band widening *Eng. Struct.* **275** 115091

[82] Alshaqaq M and Erturk A 2020 Graded multifunctional piezoelectric metastructures for wideband vibration attenuation and energy harvesting *Smart Mater. Struct.* **30** 015029

[83] Manzoni S, Moschini S, Redaelli M and Vanali M 2012 Vibration attenuation by means of piezoelectric transducer shunted to synthetic negative capacitance *J. Sound Vib.* **331** 4644–57

[84] Berardengo M, Manzoni S, Thomas O and Vanali M 2018 Piezoelectric resonant shunt enhancement by negative capacitances: optimisation, performance and resonance cancellation *J. Intell. Mater. Syst. Struct.* **29** 2581–606

[85] Sato H 1983 Free vibration of beams with abrupt changes of cross-section *J. Sound Vib.* **89** 59–64